Bioactive Materials 9 (2022) 428–445

Contents lists available at ScienceDirect

Bioactive Materials

journal homepage: www.sciencedirect.com/journal/bioactive-materials

Photothermal therapy with regulated Nrf2/NF-κB signaling pathway for treating bacteria-induced periodontitis

Yujuan Tian [a], Ying Li [a,**], Jialin Liu [a], Yi Lin [a], Jian Jiao [a], Bo Chen [a], Wanmeng Wang [a], Shuilin Wu [b,*], Changyi Li [a,***]

[a] School of Dentistry, Stomatological Hospital, Tianjin Medical University, Tianjin, 300070, People's Republic of China
[b] School of Materials Science & Engineering, Key Laboratory of Advanced Ceramics and Machining Technology by the Ministry of Education of China, Tianjin University, Tianjin, 300072, People's Republic of China

ARTICLE INFO

Keywords:
Periodontitis
Prussian blue
Photothermal therapy
Nrf2/NF-κB signaling pathway
Bacterial infection

ABSTRACT

Periodontitis is an inflammatory disease initiated by bacterial infection, developed by excessive immune response, and aggravated by high level of reactive oxygen species (ROS). Hence, herein, a versatile metal-organic framework (MOF)-based nanoplatform is prepared using mesoporous Prussian blue (MPB) nanoparticles to load BA, denoted as MPB-BA. The established MPB-BA nanoplatform serves as a shelter and reservoir for vulnerable immunomodulatory drug BA, which possesses antioxidant, anti-inflammatory and anti-bacterial effects. Thus, MPB-BA can exert its antioxidant, anti-inflammatory functions through scavenging intracellular ROS to switch macrophages from M1 to M2 phenotype so as to relieve inflammation. The underlying molecular mechanism lies in the upregulation of phosphorylated nuclear factor erythroid 2-related factor 2 (Nrf2) to scavenge ROS and subsequently inhibit the nuclear factor kappa-B (NF-κB) signal pathway. Moreover, MPB-BA also exhibited efficient photothermal antibacterial activity against periodontal pathogens under near-infrared (NIR) light irradiation. *In vivo* RNA sequencing results revealed the high involvement of both antioxidant and anti-inflammatory pathways after MPB-BA application. Meanwhile, micro-CT and immunohistochemical staining of *p*-Nrf2 and p-P65 further confirmed the superior therapeutic effects of MPB-BA than minocycline hydrochloride. This work may provide an insight into the treatment of periodontitis by regulating Nrf2/NF-κB signaling pathway through photothermal bioplatform-assisted immunotherapy.

1. Introduction

Periodontitis is a chronic inflammatory disease that affects ≈10 % population in the world [1]. It is initiated by periodontal bacterial infections and subsequently aggravated by overreacting host immune response [2]. If not treated promptly and effectively, periodontitis will lead to connective tissue degradation, alveolar bone resorption, and even teeth loss, which diminish the quality of life extremely [3]. In addition, periodontitis is related to the progress of systemic diseases such as diabetes mellitus, Alzheimer's disease, cardiovascular diseases, preterm birth, rheumatoid arthritis, chronic kidney disease, and cancers [4–10]. The longer duration of inflammation contributes to a higher risk of oral and systemic diseases. Hence, developing a rapid and effective strategy to relieve inflammation is central to the therapy of bacteria-induced periodontitis.

Nowadays effectively alleviating inappropriate inflammation and rapidly eradicating pathogenic bacteria simultaneously are two challenges in the treatment of periodontitis. Periodontitis is a physiological defense to fight against pathogens such as bacteria and viruses [11,12]. However, periodontitis occurs when the immune system failed to inhibit oral bacterial infections and excessive local inflammatory response with the disrupted bacteria-host balance can lead to periodontal tissue damage [13–16]. In the pathogenesis of periodontitis, oxidative stress is an inseparable part, which is a consequence of aggravated inflammation caused by excessive production of reactive oxygen species (ROS) [17,18]. A high level of ROS creates an inflammatory microenvironment to

Peer review under responsibility of KeAi Communications Co., Ltd.
* Corresponding author.
** Corresponding author.
*** Corresponding author.
E-mail addresses: yingli@tmu.edu.cn (Y. Li), shuilin.wu@gmail.com, shuilinwu@tju.edu.cn (S. Wu), lichangyi@tmu.edu.cn (C. Li).

https://doi.org/10.1016/j.bioactmat.2021.07.033
Received 17 June 2021; Received in revised form 29 July 2021; Accepted 29 July 2021
Available online 5 August 2021

sustain macrophages in the M1 phenotype, which exacerbates inflammation *via* releasing pro-inflammatory cytokines and ROS [19,20]. Besides, excessive ROS directly leads to oxidative damage to periodontal tissue *via* cellular lipid peroxidation and destruction of protein and DNA to impair periodontal tissue regeneration [21]. Therefore, employing antioxidant agents to scavenge ROS so as to alleviate overburdened inflammation have been considered a promising way for blocking the progression of the periodontitis, especially in case where initial periodontal treatment fails to relieve inflammation.

Currently, several antioxidant drugs have been used to alleviate the inflammation pathological degree of periodontal tissue *via* reconstruction of the redox homeostasis and regulation of immune responses [22–25]. Among them, baicalein (BA) is a US Food and Drug Administration (FDA)-approved antioxidant, which demonstrates pharmacological activities of antioxidant, anti-inflammatory, and anti-bacterial effects in both *in vitro* and *in vivo* experiments [26–28]. Nevertheless, low solubility, bioavailability, chemical stability, and short half-life severely limit the biomedical application of BA [29]. Thus, drug delivery platforms are required to enhance the stability and efficiency of BA.

Recently, Metal-organic framework (MOF) nanoparticles have been widely used as drug carriers, which can load and delivery BA to protect it from hydrolysis in a highly complicated microenvironment, thereby improving its bioavailability at the inflammation site. Additionally, MPB can control release of BA under NIR light irradiation. MOF nanoparticles are porous crystalline material comprising metal ions and organic ligands through coordination bonds. In biomedicine, MOFs are extensively used as drug carriers because of the large specific surface area, porosity, and chemical stability [30]. Prussian blue (PB) is one of the MOFs which have been approved by the FDA and widely used in biomedical applications owing to its excellent biosafety and biocompatibility [31–35]. Mesoporous Prussian blue (MPB) may serve as a potential nanoplatform for BA loading due to its larger specific areas and higher drug loading potency than PB [36]. MPB also possesses enzyme-like activity (nanozymes), which is important in ROS scavenging process for antioxidant therapy [37–40]. Compared with natural enzymes, MPB nanozyme has the advantage of low cost, stability, and capacity for mass production [41–43].

An ideal drug for periodontitis treatment should also possess desirable antibacterial activity. Clinically, dental plaque is mainly eliminated by antibiotics adjunct to mechanical debridement [44]. Due to bacterial resistance caused by the abuse of antibiotics, new alternative antibacterial strategies are needed urgently. Photothermal therapy (PTT) exhibits good antibacterial performance in the presence of local heat production (usually more than 50 °C) under near-infrared (NIR) light irradiation to destroy bacteria *via* membrane damage and protein denaturation [45]. However, high temperature is unfavorable for adjacent healthy tissue and low temperature may not achieve ideal antibacterial effect, which posed a dilemma when using PTT alone to kill bacteria [46,47]. In response to this challenging dilemma, the combination of PTT with antibacterial drugs becomes a promising approach to improve antibacterial efficiency without affecting surrounding normal tissue. Among the photothermal agents that could be engaged in PTT, MPB possesses good stability under NIR light irradiation [48,49].

In view of the above-mentioned factors, we propose a hypothesis if the MPB-based system can be constructed to regulate the phenotype of macrophages and release BA controllably under NIR light irradiation, thus achieving effective treatment of bacteria-induced periodontitis through the synergy of photothermal therapy, nanozyme and immunotherapy.

Based on the hypothesis, herein, the MPB-BA system is prepared to fulfill the combined antioxidant, anti-inflammatory and anti-bacterial effects. MPB-BA can attenuate oxidative stress and excessive inflammation effectively and eliminate periodontal pathogenic bacteria rapidly. MPB-BA can scavenge intracellular ROS and shift macrophage phenotype from M1 towards M2 to relieve inflammation. Furthermore, the underlying mechanism are also investigated. MPB-BA enhances the phosphorylation ability of phosphorylated nuclear factor erythroid 2-related factor 2 (*p*-Nrf2) to inactivate the nuclear factor kappa-B (NF-κB) signaling pathway, with downregulation of phosphorylated I-kappa B kinase beta (*p*-IKKβ) and nuclear factor-kappa B P65 (p-P65). At the same time, PTT acted with BA to kill bacteria synergistically. For detailed mechanism, please refer to Scheme 1.

2. Materials and methods

2.1. Materials

Potassium ferricyanide (K_3 [Fe $(CN)_6$]) and baicalein (BA) were bought from Aladdin (China). Hydrochloric acid (HCl, 36.0 %–38.0 %) and Poly (vinylpyrrolidone) (PVP, K30) were bought from Sinopharm Chemical Reagent Co., Ltd. All materials and reagents were applied directly without further purification.

2.2. Synthesis of mesoporous Prussian blue

3.0 g PVP, 132 mg K_3 [Fe $(CN)_6$], and 40 mL HCl solution (0.01 M) were mixed and stirred until clarified. Next, the obtained solution was poured into the reaction kettle, which was put into electric oven (80 °C, 20 h). Then, the synthesized samples were centrifuged (10,000 rpm, 15 min) and washed with ethanol and distilled water for three times. Mesoporous Prussian blue (MPB) nanoparticles were collected after drying for further use.

2.3. Synthesis of MPB-BA

25 mL of BA in PBS solution (1 mg mL^{-1}) was added to 25 mL of MPB (4 mg mL^{-1}) in PBS solution at room temperature and stirred continuously for 24 h. Centrifugation (12,000 rpm, 8 min) were performed to collect the precipitates. After washing with PBS several times, nanoparticles were obtained after drying, denoted as MPB-BA, for further use.

2.4. Synthesis of Cy5-MPB-BA

Cy5, a fluorescent dye, was encapsulated into MPB-BA to marked it with red fluorescence, denoted as Cy5-MPB-BA. In brief, the Cy5 dispersed in methanol were added to the MPB-BA solution in methanol, and the mixture was sonicated for 15 min. Next, this mixture was stirred for 12 h and then centrifuged at 12,000 rpm for 30 min. After washing with PBS several times, Cy5-MPB-BA nanoparticles were collected for the following test.

2.5. Characterization

Field-emission scanning electron microscope (FESEM, Hitachi S-4800, Japan) was applied to analyze the morphology of the samples. The particle size of MPB and MPB-BA was obtained by analyzing the images taken by SEM. High-resolution transmission electron microscope (HRTEM; JEM-2100F, Japan) was applied to measure the morphology and structure of the samples. The crystal structure of the samples was investigated by X-ray diffraction (XRD, Haoyuan Instrument Co., Ltd., China). Fourier transform infrared (FTIR) spectroscopy was examined by an FTIR spectrometer (Thermo Scientific, USA). Raman spectroscopy was detected using DXR Raman microscope (Thermo Scientific, USA) equipped with a DXR 532 nm laser. X-ray photoelectron spectroscopy (XPS, Axis Supra, UK) was used to investigate the elemental chemical states. UV–Vis–NIR absorption was measured using a microplate reader (Bio-TEK Instrument, USA). Brunauer-Emmett-Teller (BET, Micromeritics, 3Flex, USA) method was used to calculate the specific surface area. Nitrogen desorption branch was applied to analyze The pore volume and pore width were calculated according to the Barrett-Joyner-Halenda (BJH) method.

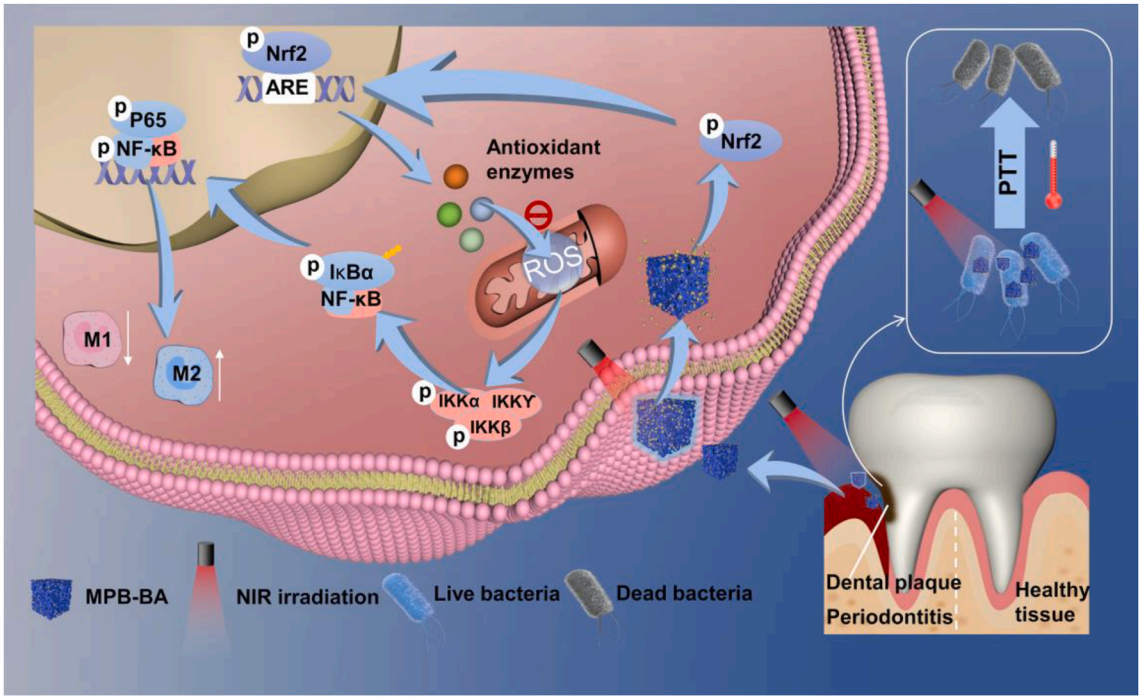

Scheme 1. Schematic illustration of antioxidant, anti-inflammatory mechanism and antibacterial effects of MPB-BA in the treatment of periodontitis.

2.6. Evaluation of photothermal properties of MPB-BA

The temperature trends of different power (0.5, 1.0, and 1.5 W cm^{-2}) of MPB-BA (100 p.p.m.) dispersed in PBS solution were measured under irradiation with an 808 nm NIR light (Hi-Tech Optoelectronics Co., Ltd., China). Different concentrations (50, 100, 200, and 400 p.p.m.) of MPB and MPB-BA solutions were dispersed in PBS in an EP tube (Eppendorf tube). Then MPB and MPB-BA solutions with different concentrations were irradiated by 808 nm NIR laser at 1.0 W cm^{-2} for 5 min, with temperature measured. Pure PBS was used as control group (Ctrl). In the meantime, the photothermal stability of MPB and MPB-BA was examined by an ON/OFF cycle experiment under 808 nm NIR light irradiation. In brief, the MPB and MPB-BA dispersion was first irradiated under an 808 nm laser at 1.0 W cm^{-2} for 5min, then allowed to cool to the initial temperature naturally. The other two cycles were repeated and measured in the same way. Temperature trends were recorded using a FLIR thermal camera (FLIR-E50, USA). The photothermal conversion efficiency (η) of MPB-BA was calculated according to equation. (1):

$$\eta = \frac{hS(T_{\max} - T_{amb}) - Q_0}{I(1 - 10^{-A})},$$

h represents the heat transfer coefficient, Q_0 represents the heat absorption of EP tube, S represents the surface area of the tube, *Tmax* represents the equilibrium temperature, *Tamb* represents the surrounding ambient temperature, I represents the laser power and A is the absorbance of MPB-BA at 808 nm.

If the heat input of the system equals to the heat output,

$$hS = \frac{\sum_i m_i C_{p,i}}{\tau_S} \approx \frac{m_{H_2O} C_{H_2O}}{\tau_S}.$$

Among the equation, m_{H2O} represents the weight of water, C_{H2O} represents the specific heat capacity of water and τ_S represents the time constant of MPB-BA. During the cooling period,

$$t = -\tau_S \ln \theta = -\tau_S \ln \frac{T - T_{amb}}{T_{\max} - T_{amb}}.$$

τ_S can be calculated accroding to the linear regression curve.

2.7. In vitro evaluation of NIR-controlled release of BA

UV–Vis–NIR absorption of BA (0.5, 1, 2, 5, 12.5, 25, 50, and 100 p.p.m.) was examined using a microplate reader (Bio-TEK Instrument, USA). The linear relationship between concentrations and absorbance was calculated. BA release from MPB-BA (100 p.p.m.) dispersed in PBS was investigated at 37 °C at different time points (0 h, 2 h, 6 h, 12 h, day 1, and day 3). The resultant samples were centrifuged (10,000 rpm, 10 min) to remove MPB-BA to avoid interference during detection. Then, the absorbance of 100 μL supernatant was measured at 259 nm by microplate reader (Bio-TEK Instrument, USA). To verify whether the 808 nm NIR laser irradiation can manipulate the release of BA, the subjects were distributed into 3 groups: 72-h darkness (Dark Group); 0-h-point irradiation for 15 min, 15 min-point to 72-h darkness (0 h Group); 0-h-point irradiation for 15 min, 15 min-point to 2-h darkness, 2-h-point irradiation for15 min, darkness until 72-h (0 h + 2 h Group). BA release behavior was examined as described above. The cumulative release concentration of BA was calculated according to the linear relationship between concentrations and absorbance obtained at 259 nm. Cumulative release percentage was calculated by the cumulative concentration of BA.

2.8. Evaluation of ROS scavenging activities of MPB-BA

For a total antioxidant capacity assay of MPB-BA, 2,2-azino-bis-3-ethylbenzothiazoline-6-sulfonic acid (ABTS) radical cation scavenging test was examined by the ABTS radical cation scavenging kit (Beyotime Biotechnology, China). A sample (10 μL) at the final concentration of 50, 100, 200, and 400 p.p.m. for MPB, 5, 12.5, 25, and 50 p.p.m for BA, and 50, 100, 200, and 400 p.p.m. for MPB-BA was mixed with 170 μL of ABTS solution. The mixture was reacted at room temperature for 6 min. Then the absorbance of the solution was measured at 414 nm. Meanwhile, Trolox was used as a reference and ABTS radical scavenging activity of MPB, BA and MPB-BA was denoted by Trolox-Equivalent Antioxidant Capacity (TEAC).

For the catalase-like activity (CAT-like) of MPB-BA, the CAT-like activity assays of MPB (50, 100, 200, and 400 p.p.m.), BA (5, 12.5, 25, and 50 p.p.m), and MPB-BA (50, 100, 200, and 400 p.p.m.) were

carried out by the CAT-like activity kit (Nanjing Jiancheng Bioengineering Institute, China). The absorbance of the color reaction at 240 nm for decomposition of H_2O_2 was recorded at a certain reaction time *via* a microplate reader (Bio-TEK Instrument, USA).

Moreover, quantitative production of O_2 was further detected by a dissolved oxygen meter (JPB-607A, China). Briefly, 0.8 M H_2O_2 solution was incubated with MPB (50, 100, 200, and 400 p.p.m.), BA (5, 12.5, 25, and 50 p.p.m), and MPB-BA (50, 100, 200, and 400 p.p.m.), separately. Oxygen solubility was recorded after the reaction for 2 min.

2.9. Cellular uptake study

Macrophage cells were seeded into 12-well plates at a density of 1×10^4 cells per well. After culturing for 24 h, cells were treated by lipopolysaccharide (LPS, 1 μg mL^{-1}) for 6 h at naked Cy5 and MPB-BA groups. Subsequently, cells were treated with Cy5 and Cy5-labeled MPB-BA for 4 h. After being rinsed by PBS 3 times, macrophage cells were fixed with 4 % paraformaldehyde solution for 10 min followed by rinsing with PBS. The nucleus was stained by DAPI for 5 min. Internalization of materials was obtained *via* laser scanning confocal microscopy (LSCM, Olympus, FV1000, Japan). To further analyze the internalization of materials quantitatively, macrophage cells were seeded into 6-well plates at a density of 4×10^5 cells per well. The cells were treated as steps described above. Then macrophage cells were washed by PBS and fixed in 2 % paraformaldehyde. The fluorescence intensity of collected cells was detected by flow cytometry (BD FACSVerse, USA). Mean fluorescence intensity (MFI) was calculated to quantitatively analyze the intensity of Cy5.

2.10. In vitro biocompatibility of MPB, BA, and MPB-BA in macrophages

RAW 264.7 (mouse peritoneal macrophages) cells were obtained from the ATCC (ATCC TIB-71, USA). Cells were cultured in Dulbecco's Modified Eagle Medium (DMEM, HyClone, USA), with 10 % fetal bovine serum (FBS, Gibco, USA) and 1 % penicillin/streptomycin in a 5 % CO_2 atmosphere at 37 °C.

For cell proliferation assessment, macrophage cells treated with MPB and BA, were determined by the Cell Counting Kit-8 (CCK-8, New Cell & Molecular Biotech, China) assay at various concentrations. Macrophage cells (1×10^3 per well) were seeded in 96-well plates and cultured for 24 h. Then the culture medium was replaced by the fresh medium with different concentrations of MPB (50, 100, 200, and 400 p.p.m.) and BA (0.5, 1, 2, 5, 12.5, 25, 50, and 100 p.p.m.) for 24 h. After that, fresh medium was replaced every day. Control (Ctrl) group was treated with fresh medium containing PBS. After incubation for 1, 3, 5 and 7 days, cells were washed by PBS for 3 times. Fresh medium (90 μL) containing CCK-8 solution (10 μL) was added into the wells and cultured for 1 h. Absorbance values at 450 nm were examined by a microplate reader (Bio-TEK Instrument, USA).

To investigate the effect of near-infrared (NIR) light irradiation on cell viability, the cells containing MPB, BA, and MPB-BA were test by CCK-8 assay. Macrophage cells treated with Ctrl (PBS), MPB (100 p.p.m.), BA (25 p.p.m.) and MPB-BA (100 p.p.m.) were irradiated for 5 min to reach 50 °C. Then, samples were irradiated for another 10 min to maintain the temperature between 50 °C and 55 °C. And then cells were treated as described above. Cell viabilities were calculated by the formula: cell viability = OD test/OD control.

2.11. In vitro antibacterial efficacy of MPB-BA after laser irradiation

Antibacterial activity of MPB-BA against *Porphyromonas gingivalis* (*P. gingivalis*, ATCC 33277, USA) and *Fusobacterium nucleatum* (*F. nucleatum*, ATCC 25586, USA) was measured by the spread plate assay quantitatively. The bacteria were cultured with brain heart infusion broth (BHI, Sigma-Aldrich, USA) supplemented menadione (1 mg L^{-1}, Sigma-Aldrich, USA), L-cysteine hydrochloride (0.5 g L^{-1}, Sigma-Aldrich, USA), yeast extract (5 g L^{-1}, Sigma-Aldrich, USA), and hemin (5 mg L^{-1}, Sigma-Aldrich, USA) and BHI agar supplemented menadione (1 mg L^{-1}, Sigma-Aldrich, USA), hemin (5 mg L^{-1}, Sigma-Aldrich, USA), and 5 % defibrinated sheep blood (Solarbio, China) at 37 °C anaerobically with 80 % N_2, 10 % H_2 and 10 % CO_2. Next, 200 μL bacterial suspensions at the density of 6×10^6 Colony-Forming Units (CFU)·per milliliter were incubated with Ctrl (PBS), MPB (100 p.p.m.), BA (25 p.p.m.), and MPB-BA (100 p.p.m.) in a 96-well plate with an 808 nm NIR light irradiation. Initially samples were irradiated for 5 min to reach 50 °C. Then, samples were irradiated for another 10 min to maintain the temperature between 50 °C and 55 °C. After 2-h incubation in darkness, 20 μL of the appropriate diluted bacterial solution was plated on blood agar and incubated anaerobically for 7 days of *P. gingivalis* and 5 days of *F. nucleatum*. Three independent experiments were performed. The bacterial colonies were recorded, and the antibacterial ratio was calculated using the follwing formula: Antibacterial ratio (%) = (A−B)/A × 100, where A represents the average numbers of bacteria colonies for the Ctrl group (CFU per sample), and B represents the average numbers of bacteria colonies for the experimental group (CFU per sample).

Ortho-nitrophenolgalactoside (ONPG) membrane permeabilization assay was performed to assess the antibacterial activity of MPB-BA. 200 μL bacterial suspensions (6 × 106 CFU mL-1) were incubated with Ctrl (PBS), MPB (100 p.p.m.), BA (25 p.p.m.), and MPB-BA (100 p.p.m.) in a 96-well plate with an 808 nm NIR light irradiation. Especially, the irradiated temperature was more than 50 °C after 5 min and maintained between 50 °C and 55 °C for the following 10 min. 1.25 mM of ONPG (Beyotime Biotechnology, China) was added to a 96-well plate. The relative ONPG hydrolysis intensity was measured by a microplate reader at λ = 420 nm.

The morphology of *P. gingivalis* and *F. nucleatum* cultivated with Ctrl and MPB-BA was observed by SEM after irradiation. Firstly, samples were irradiated by 808 nm NIR light for 5 min to reach 50 °C. Then, samples were irradiated for another 10 min to maintain the temperature between 50 °C and 55 °C. After 2-h incubation in darkness, the treated bacteria were fixed with 2.5 % glutaraldehyde solution (2 h) and then rinsed by PBS for three times. Next, the treated bacteria were gradually dehydrated in ethanol of different concentrations (30, 50, 70, 90, and 100 %, v/v) for 15 min, respectively. Finally, the dehydrated bacteria were dried overnight followed by gold sputtering before SEM observation.

2.12. The effects of MPB-BA on macrophage polarization

For immunofluorescence staining, macrophage cells were seeded in 24-well plates (1×10^5 cells per well). Macrophage cells in MPB, BA, MPB-BA and MPB-BA with laser irridiation groups were pretreated by medium with MPB (100 p.p.m.), BA (25 p.p.m.), MPB-BA (100 p.p.m.) and MPB-BA (100 p.p.m.) for 24 h, respectively. Besides, MPB-BA (100 p.p.m.) with laser irridiation group was irridiated with an 808 nm NIR light. Especially, the irradiated temperature was more than 50 °C after 5 min and maintained between 50 °C and 55 °C for the following 10 min. Then cells in lipopolysaccharide (LPS), MPB, BA, MPB-BA, and MPB-BA with laser irridiation groups were activated by LPS (Sigma-Aldrich, USA) at a final concentration of 1 μg mL^{-1} for 6 h to induce inflammatory status. After rinsed by PBS for 3 times, macrophage cells were fixed with 4 % paraformaldehyde solution for 10 min followed by rinsing with PBS. Then, the samples were blocked with BSA at room temperature for 1 h and incubated with CCR-7 (M1 marker, 1:100 dilution, Abcam) and CD206 (M2 marker, 1:100 dilution, Abcam) primary antibodies at 4 °C overnight. After washing with PBS, the samples were incubated with FITC-labeled goat anti-rabbit IgG antibodies (1:200 dilution, Invitrogen). Cell nuclei were stained with 4′, 6-diamidino-2-phenylindole (DAPI, Beyotime Biotechnology, China). Cytoskeleton was stained with a TRITC-conjugated *anti*-F-actin antibody (1:200, Life Technologies). Images were obtained *via* laser scanning confocal

microscopy (LSCM, Olympus, FV1000, Japan).

To confirm the expression of macrophage markers quantitatively, flow cytometric analysis was performed. Macrophage cells were seeded in 6-well plates (5×10^5 cells per well). Macrophage cells were treated as described above. After incubation, cells were scraped off and centrifuged (1000 rpm, 5 min). After resuspension, macrophage cells were incubated with CCR-7 antibody (1:100 dilution, Abcam) and CD206 antibody (1:100 dilution, Abcam), respectively on ice in the dark for 30 min. After washing with PBS, the cells were cultured with Alexa Fluor 647, Goat anti-Rabbit IgG (H + L) Cross-Adsorbed Secondary Antibody (1:200 dilution, Invitrogen) on ice in the dark for 30 min. Finally, macrophage cells were washed and fixed in 2 % paraformaldehyde. Flow cytometry (BD FACSVerse, USA) was used to analyze the phenotype of macrophage cells. Each analysis was performed for three times. The results were analyzed with FlowJo software (Tree Star, Version 7.6, CA). Mean fluorescence intensity (MFI) was calculated to quantitatively analyze the expression of CCR-7 and CD206.

2.13. In vitro antioxidant and anti-inflammatory effects of MPB-BA

The intracellular ROS production was detected using 2,7-dichlorodihydrofluorescein diacetate (DCFH-DA, Sigma-Aldrich, USA). Mcrophage cells were inoculated in a black 96-well plate with at a density of 10^4 per well for 24 h. After treated as described above, the cell medium was replaced with 10 μmol L^{-1} DCFH-DA followed by incubation in the dark for 0.5 h at 37 °C. Intracellular DCF fluorescence was measured at 488 nm for excitation and 525 nm for emission by a fluorescence microplate reader (Bio-TEK Instrument, USA) and quantified.

The mRNA expression of antioxidant antioxidative genes (*SOD-1*, *CAT*, *NQO-1*, and *HO-1*) was also measured through quantitative Realreal-time polymerase chain reaction PCR (qRT-PCR) assay. Macrophage cells were plated on 6-well plates (5×10^5 cells per well) and then treated as described above in the part of *The effects of MPB-BA on macrophage polarization*. Total RNA from macrophage cells was extracted with TRIzol reagent (Invitrogen, USA). cDNA was obtained using All-In-one RT Master Mix (abm, USA). The expressions of the inflammatory genes were detected by qRT-PCR in a Bio-Rad CFX96™ Detection System (Roche, Sweden) with SYBR PCR Master Mix (Roche, USA). The primer sequences used are shown in Table S1.

To measure the anti-inflammatory effect of MPB-BA, the mRNA expression of inflammation-related genes (*IL-1β, TNF-α, iNOS, TGF-β, IL-10*, and *Arg-1*) were measured using a qRT-PCR assay. Macrophage cells were treated as described above in the part of *The effects of MPB-BA on macrophage polarization*. The experimental steps were the same as above. The primer sequences used are shown in Table S2.

2.14. In vitro antioxidant and anti-inflammatory mechanism of MPB-BA by regulating the Nrf2/NF-κB pathway

The expression of phosphorylation of nuclear factor erythroid-2 related factor 2 (*p*-Nrf2) and location of *p*-Nrf2 were examined by immunofluorescence staining. Macrophage cells were cultured in a 24-well plate (1×10^5 cells per well). Macrophage cells pretreated by medium with MPB-BA (at the final concentration of 100 p.p.m.) for 24 h and then stimulated by LPS (1 μg mL^{-1}) for 0, 30, and 60 min were denoted as the MPB-BA (+) group. Macrophage cells directly stimulated by LPS (1 μg mL^{-1}) for 0, 30, and 60 min were denoted as the MPB-BA (+) group. Then macrophage cells were rinsed by PBS, cells were fixed in 4 % paraformaldehyde for 10 min. Then, macrophage cells were washed by PBS and incubated with an *anti-p*-Nrf2 antibody (1:100 dilution, Affinity) for 12 h at 4 °C. After washing with PBS, the samples were cultured with FITC-labeled goat anti-rabbit IgG antibodies (1:200 dilution, Invitrogen). Cell nuclei were stained with DAPI (Beyotime Biotechnology, China). Images were captured *via* LSCM (Olympus, FV1000, Japan).

Western blot analysis was used to detect the related expression levels of antioxidant protein (*p*-Nrf2 and Nrf2), NF-kB signal pathway proteins (*p*-IKKβ, IKKβ, p-P65, and P65), and glyceraldehyde 3-phosphate dehydrogenase (GAPDH). Macrophage cells were treated as described above in this part. The total proteins were extracted using a radioimmunoprecipitation (RIPA) buffer (Millipore, USA) on ice. RIPA buffer-extracted lysates were sonicated and centrifuged at 12,000 rpm. Sodium dodecyl sulfate-polyacrylamide gel electrophoresis (SDS-PAGE) was used to separate the proteins, and then the proteins were transferred to a polyvinylidene fluoride (PVDF) membrane (Millipore, USA). 5 % dehydrated milk dissolved in PBS was used to block the membranes at room temperature for 1 h. PVDF membranes with proteins were sequentially incubated with *p*-Nrf2 (S40) (1:2000, Affinity), Nrf2 (1:2000, proteintech), *p*-IKKβ (1:1000, Cell Signaling Technology), IKKβ (1:1000, Cell Signaling Technology), NF-κB p-P65 (1:1000, Cell Signaling Technology), NF-κB P65 (1:1000, Cell Signaling Technology), and glyceraldehyde 3-phosphate dehydrogenase (GAPDH, 1:5000, Cell Signaling Technology) primary antibodies at 4 °C overnight. Then, PDVF membranes containing proteins were incubated with a secondary antibody (1:8000 dilution, Abways) for 1 h at room temperature. Finally, the membranes were exposed using an ECL kit (CWBIO, China) to visualize the immunoreactive protein bands. Protein bands were analyzed using Image-pro Plus J software (Media Cybernetics, ver.5.0, USA).

2.15. Animal and surgical experiment

The experiment in this study were approved by the Animal Ethics Welfare Committee (AEWC) of Tianjin Hospital of Itcwm Nankai Hospital (approval no. NKYY-DWLL-2020-093). Fourty-two male Sprague−Dawley rats (2-month-old, 250–300 g) were used fot animal experiment. Among them, thirty-six rats were used for hematoxylin and eosin (H&E) staining and microcomputed tomography (micro-CT) analysis, while six rats were used for RNA-seq analysis. Fourty-two rats were randomly divided into 4 groups (n = 12 for periodontitis group and MPB-BA group; n = 9 for Min group and Ctrl group). SD rats were anesthetized with pentobarbital sodium (50 mg kg^{-1}), after that a 4-0 silk ligature was tied around the cervix of the left maxillary second molar. A high-sugar diet (sugar syrup, 100 g L^{-1}) was also provided to rats every day to accelerate the periodontitis establishment. The mixture of *P. gingivalis* and *F. nucleatum* bacterial suspension (10^7 CFU mL^{-1}, 10 μL) was injected into the gingival sulcus around left maxillary second molar every other day and four times of injections in total. Silk ligature was remained for 30 days to induce periodontitis. After ligature removal, PBS was injected into periodontal pocket named as periodontitis group. MPB-BA (100 p.p.m) was injected into periodontal pocket with irradiation by 808 nm NIR light for 15 min and the temperature changes were monitored by a FLIR thermal camera (FLIR-E50, USA), named as MPB-BA group. Minocycline Hydrochloride Ointment, the most commonly used antibiotic for current clinical treatment of periodontitis (Min, 2 % minocycline hydrochloride, Sunstar, Japan) was injected and the dose was appropriate to fill periodontal pocket as a positive control, named as Min group. Ctrl group was with healthy rat without treatment. Animals were sacrificed at denoted time point and samples from each group were harvested for further analysis. Nine rats from each group were used for H&E staining and micro-CT analysis, while three rats from the periodontitis group and MPB-BA group, respectively were used for RNA-seq analysis.

2.16. In vivo biodistribution and pharmacokinetics of MPB-BA

The periodontitis rat was treated with Cy5 labeled MPB-BA and the maxillary with gingival of rats was collected and imaged *via* a VIS *in vivo* imaging system (PerkinElmer, Waltham, USA) after 10 h.

For the pharmacokinetics of MPB-BA, the urine and feces of Cy5-MPB-BA treated rats were collected at 12 h, 24 h, 36 h, 48 h, and 72 h post-treatment. These samples were treated by a high-pressure

microwave oven. Afterward, samples were digested by aqua regia, followed by heating to removes organic contents completely. The Fe content was measured quantitatively by ICP-MS (Agilent 7500C).

2.17. In vivo therapeutic mechanism of MPB-BA for periodontitis

For RNA-seq analysis, six rats from the periodontitis group and MPB-BA group (n = 3 for each group) were sacrificed after 3 days of treatment. The gingival tissue around the maxillary second molar of animals was collected and preserved in liquid nitrogen after cuting into small fragments. Total RNA was extracted using TRIzol reagent (Invitrogen, USA). The purity and the concentration of RNA were measured using Nanodrop 2000c (Thermo Scientific, USA). Qualified RNA was stored at −80 °C for sequencing using Illumina HiSeq X10 (Illumina, USA). The RNA sequencing results were analyzed by free online Majorbio Clound Platform (www.majorbio.com).

Gene Ontology (GO) and Kyoto Encyclopedia of Genes and Genomes (KEGG) pathway analysis were used for transcriptome analysis. The GO database (http://geneontology.org/) was used to analyze the differentially expressed genes enriched in the main function in accordance with the gene ontology. Pathway analysis was employed to analyze the significant pathways with differential genes between different samples according to the KEGG database (http://www.genome.jp/kegg/). In this study, Fisher's exact test and the χ2-test were used for GO and KEGG pathway analysis. The p-value was corrected using false discovery rate (FDR) method.

2.18. In vivo therapeutic efficacy of MPB-BA for periodontitis

Before the experiment, the gingival tissues from sacrificed animals after different treatments for 3 days and 7 days were collected for anti-inflammatory evaluation by H&E staining. A semi-quantitative scoring system was applied to measure inflammatory cells of the affected gingival tissue. In the score system, 0, 1, 2 and 3 represented the negative control, less than 30 % inflammatory cells, 30–60 % (some amount) of inflammation cells, and more than 60 % (large number) of inflammatory cells of the corresponding area, respectively [50].

For micro-CT analysis, maxillary with teeth from sacrificed animals after 30 days of treatments were collected and fixed with 4 % paraformaldehyde. Then samples were scanned using a micro-CT system (Bruker, Skyscan Company, Germany). Alveolar bone resorption was evaluated by measuring the distance between the cementoenamel junction and the alveolar bone crest (CEJ-ABC distance) according to the three-dimensional digitized images.

The gingival tissues of sacrificed animals after treatment for 7 days were collected for antioxidant (*p*-Nrf2) and anti-inflammatory (p-P65) evaluation by immunohistochemistry staining. Quantitative analysis were performed *via* Image-pro Plus J software mentioned above.

2.19. In vivo long-term toxicity test

To evaluate the safety of MPB-BA, rats were sacrificed after treatment with MPB-BA for 30 days. The main organs including heart, liver, spleen, lung, and kidney were collected and user for H&E staining.

2.20. Statistical analysis

All quantitative data were expressed as mean ± SD from at least triplicate measurements. Differences between two comparative groups were assessed using the Student's t-test, and the significance among multiple groups was examined by the one-way analysis of variance (ANOVA). Significance was measured at the following thresholds: $^{*}P < 0.05$, $^{**}P < 0.01$, $^{***}P < 0.001$, $^{****}P < 0.0001$, $^{\&}P < 0.0001$, $^{\$}P < 0.0001$, $^{\#}P < 0.0001$, $^{@}P < 0.0001$.

3. Results and discussion

3.1. Characterization of MPB and MPB-BA

Scanning electron microscope (SEM) images of MPB and MPB-BA nanoparticles showed a cubic and similarly uniform-sized structure (Fig. S1a, S1b), with an average diameter of about 133.7 nm for MPB (Fig. S2a) and 134.2 nm for MPB-BA (Fig. S2b). Transmission electron microscopy (TEM) images showed that MPB (Fig. 1a–c) and MPB-BA (Fig. 1d–f) had crystalline structures with the same calculated d space for (220). No significant differences in size and morphology were shown between MPB and MPB-BA, which indicated that the MPB nanozyme loaded with BA did not change the original crystalline structure of MPB. The elemental mapping images (Fig. 1g) of MPB-BA exhibited the uniform distribution of individual elements of Fe, C, N, and O in MPB-BA.

X-ray diffraction (XRD) patterns of MPB and MPB-BA showed characteristic peaks with high crystallinity at 17.4°, 24.8°, 35.2°, 39.4°, 43.5°, 50.7°, 53.9°, 57.1°, 66.2°, and 68.9°, corresponding to the crystal face of (200), (220), (400), (420), (422), (440), (600), (620), (640), and (642), respectively (Fig. 1h). Raman peak at 2153 cm^{-1} was ascribed to the vibrational mode of CN group and no peak shift was found between MPB and MPB-BA (Fig. 1i). The results from XRD and Raman spectroscopy suggested that the introduction of BA did not change the crystal structure of MPB. Successfully loading of BA was further confirmed by Fourier transform infrared spectroscopy (FTIR), X-ray photoelectron spectroscopy (XPS), and Brunauer-Emmett-Teller (BET) characterizations. FTIR of free BA showed peaks at 3411 cm^{-1} corresponding to OH and 1470 cm^{-1} corresponding to C—C, while MPB displayed representative absorption at 2086 cm^{-1} originated from the stretching vibration of Fe^{2+}−CN–Fe^{3+}. Moreover, MPB also showed characteristic peaks at 1646 cm^{-1} corresponding to C═O stretching from the residue of PVP amide unit. It has been reported that the C═O could form hydrogen bonds with the hydroxyl group [51]. Hence, herein, MPB bound with BA probably due to the existence of hydrogen bonds, *via* binding C═O from MPB and hydroxyl group from BA. MPB-BA showed signals from both MPB and BA fragments, confirming the successful loading of BA to original MPB nanozyme (Fig. 1j). XPS measurements were conducted to explore the chemistry of MPB and MPB-BA. The elements of C, N, O, and Fe were detected in both MPB and MPB-BA (Fig. 1k). The fitted XPS narrow scan showed two peaks at 708.6 eV and 721.5 eV for MPB assigned to Fe $2p_{3/2}$ and Fe $2p_{1/2}$, respectively. The peak intensity at 708.6 eV and 721.5 eV of MPB-BA became much weaker compared with MPB because of the existence of BA (Fig. S3a). The ratio of areas at C 1s (Fig. S3b) and O 1s (Fig. S3c) increased and that of N 1s (Fig. S3d) decreased in MPB-BA. As shown in Table S3, O 1s and C 1s contents of MPB-BA increased remarkably compared to that of MPB, which were major components of BA. Meanwhile, Fe 2p and N 1s atomic percentage of MPB-BA was lower obviously than that of MPB. These all indicated the successful superimposition of BA onto MPB. Nitrogen adsorption-desorption isotherms were displayed in Fig. 1l. The adsorbed volumes in the adsorption isotherm of MPB-BA were less than MPB, indicating the loading of BA. BET surface area decreased from 57.89 m^2 g^{-1} for MPB to 35.88 m^2 g^{-1} for MPB-BA, indicating a smaller surface roughness of the latter, due to the addition of BA. Barrett-Joyner-Halenda (BJH) desorption average pore widths were 19.74 nm for MPB and 17.14 nm for MPB-BA (Fig. 1m), which indicated that both samples possessed mesopores. The loading of BA slightly decreased the average pore widths of MPB. Besides, the MPB-BA showed a smaller total pore volume of 0.056 cm^3 g^{-1}, compared with 0.071 cm^3 g^{-1} of MPB. These results displayed that MPB-BA possessed a smaller surface area, surface pore width and pore volume compared with MPB. This phenomenon can be explained by that the loaded BA blocked the surface pores of MPB. In summary, SEM, TEM, XRD, Raman, FTIR, XPS, and BET characterizations confirmed that MPB and MPB-BA were successfully constructed.

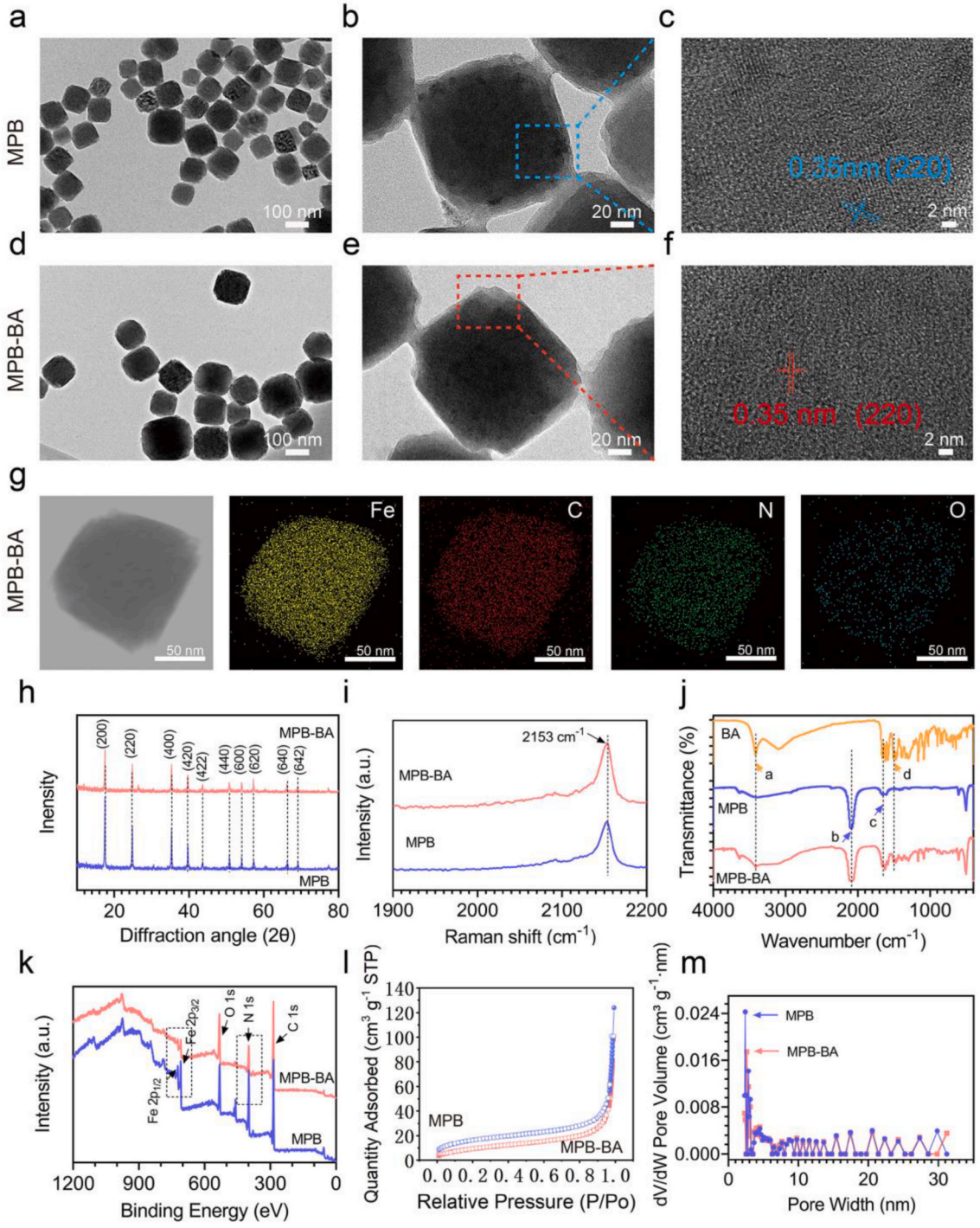

Fig. 1. Characterization of MPB and MPB-BA. (a) TEM picture of MPB, scale bar = 100 nm. (b) High-resolution TEM image of (a), scale bar = 20 nm. (c) High-resolution TEM images of the blue square shown in (b), scale bar = 2 nm. The crystal lattice planes and interplanar spacing of MPB were displayed in (c). (d) TEM picture of MPB-BA, scale bar = 100 nm. (e) High-resolution TEM image of (d), scale bar = 20 nm. (f) High-resolution TEM images of the red square shown in (e), scale bar = 2 nm. The crystal lattice planes and interplanar spacing of MPB-BA were displayed in (f). (g) Elemental mapping images of MPB-BA. (h) XRD patterns of MPB and MPB-BA. (i) Raman of MPB and MPB-BA. (j) FTIR of BA, MPB, and MPB-BA. (Inset: a represented OH at 3411 cm^{-1}; b represented Fe^{2+}–CN–Fe^{3+} at 2086 cm^{-1}; c represented C═O at 1646 cm^{-1}; d represented C—C at 1470 cm^{-1}). (k) Total peaks of XPS of MPB and MPB-BA; Fe and N elements were hilighted using dotted boxes. (l) N_2 adsorption (filled symbols) and desorption (open symbols) of MPB (blue) and MPB-BA (red). (m) Pore size distribution profiles of MPB (blue) and MPB-BA (red).

3.2. Evaluation of photothermal properties of MPB-BA

The photothermal effects of MPB-BA were investigated under 808 nm NIR light irradiation. The UV–Vis–NIR absorption spectra (300–1000 nm) of different concentrations of MPB and MPB-BA were shown in Figs. S4a and S4b. The intensities of absorbance of MPB and MPB-BA increased gradually in a concentration-dependent manner (Fig. S4c, S4d). MPB and MPB-BA showed a broad and strong absorption from 700 nm to 900 nm. As shown in Fig. 2a, the absorbance of MPB-BA hardly changed after irradiation for 5 min and followed by cooling

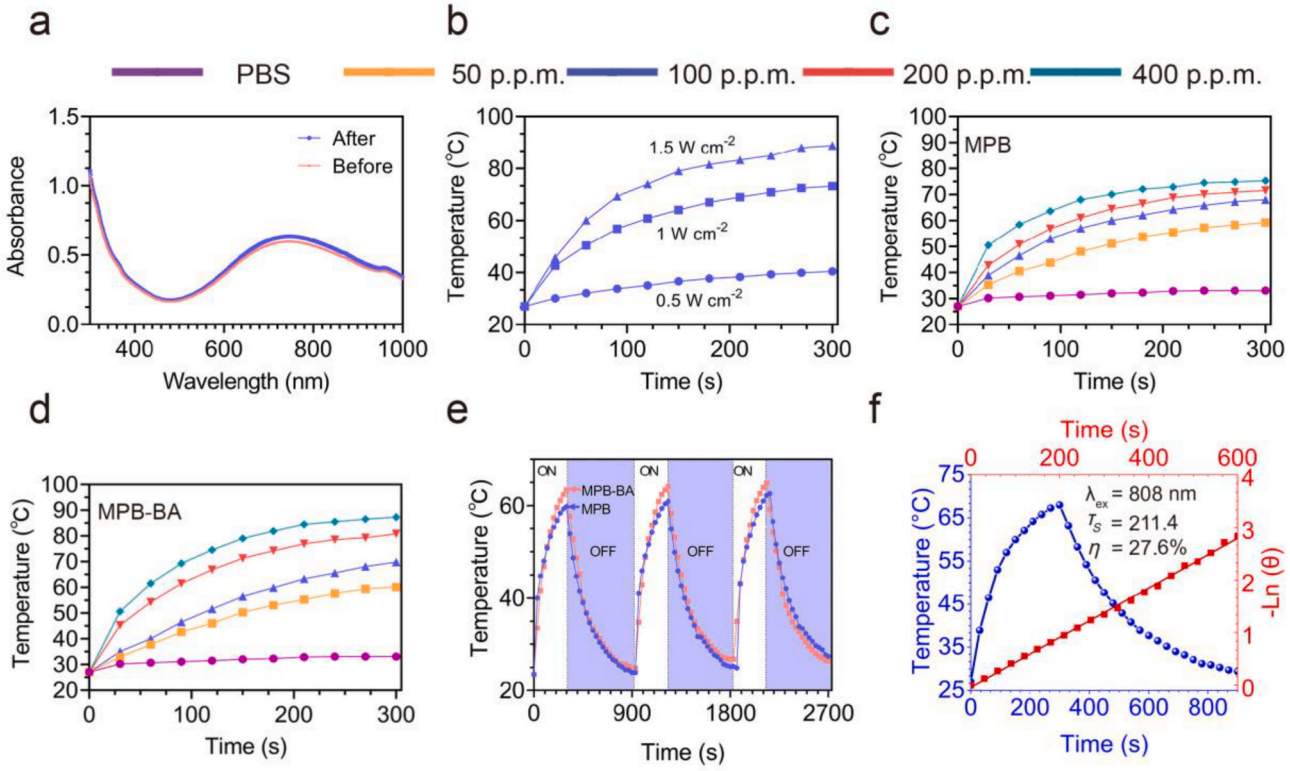

Fig. 2. Photothermal properties of MPB-BA. (a) UV–vis–NIR spectroscopy of MPB-BA (100 p.p.m.) before and after laser irradiations for three cycles. (b) Photothermal curves of MPB-BA (100 p.p.m.) irradiated by different laser intensity (0.5, 1, and 1.5 W cm^{-2}) for 5 min. Photothermal curves of MPB (c) and MPB-BA (d) with various concentrations (50, 100, 200, and 400 p.p.m.) after laser irradiation (1 W cm^{-2}) for 5 min. (e) Recycling heating profiles of MPB and MPB-BA under laser irradiation (1 W cm^{-2}) for three cycles. (f) Photothermal conversion efficiencies (η) of MPB-BA by laser irradiation for three cycles. Blue line: photothermal effect. Red line: time constant (τ_s) of the cooling period by using the linear time data.

naturally to initial temperature for 3 cycles, indicating its stable light absorption ability. Fig. 2b displayed that when MPB-BA at concentrations of 100 p.p.m. exposed to 808 nm NIR laser at a power density of 0.5, 1, and 1.5 W cm^{-2} for 5 min respectively, an apparent power-dependent temperature increase was observed. The temperature increased to 40.4 °C, 69.2 °C, and 88.8 °C after 808 nm NIR light 5-min irradiation with powder density of 0.5, 1, and 1.5 W cm^{-2}, respectively. Both MPB (Fig. 2c, Fig. S5a) and MPB-BA (Fig. 2d, Fig. S5b) displayed concentration-dependent heating curves after 1 W cm^{-2} NIR light irradiation for 5 min. The temperature of MPB-BA of various concentrations of 50, 100, 200, and 400 p.p.m. after 5 min NIR light irradiation (1 W cm^{-2}) increased to 60.1 °C, 69.8 °C, 80.8 °C, and 87.3 °C, respectively. Notably, the temperature of MPB-BA was higher than that of MPB after 5 min NIR light irradiation (1 W cm^{-2}). It has been established that the stronger light absorption ability of photothermal agents was facilitated to enhance their photothermal conversion performance [52]. Therefore, the higher absorption spectra (300–1000 nm) of MPB-BA than that of MPB at 100 p.p.m. shown in Fig. S4a and S4b may be the reason that led to the enhanced photothermal performance of MPB-BA. In contrast, the temperature of phosphate buffer solution (PBS) showed no significant change. Besides, the excellent photothermal reversibility and cycling stability of MPB and MPB-BA were displayed in Fig. 2e. Then the photothermal conversion efficiency η of MPB-BA was quantitatively calculated to be 27.6 % by the results of the time constant ($\tau_s = 211.4$) and maximum steady-state temperature, suggesting that the MPB-BA possessed the efficient photothermal conversion efficiency (Fig. 2f).

Collectively, the synthesized MPB-BA processed ideal photostability and photothermal conversion efficiency as a photothermal agent.

3.3. In vitro evaluation of NIR-controlled release of BA

The diagrams of photothermal-controlled release performance of BA were presented in Fig. 3a–c. The UV–vis absorbance spectra of BA suspensions at various concentrations (0.5, 1, 2, 5, 12.5, 25, 50, and 100 p.p.m.) were measured from 230 to 400 nm, and the maximum absorbance located at 259 nm (Fig. S6a). The absorbance values at 259 nm displayed linear dependence ($y = 147.2x - 3.474$, $R^2 = 0.9735$) with the corresponding concentrations in Fig. S6b. The linear relationship was used to calculate the concentration of BA released from MPB-BA. To explore the influence of NIR light irradiation on BA release, the subjects were distributed into 3 groups: 72-h darkness (Dark Group); 0-h-point irradiation for 15 min, 15 min-point to 72-h darkness (0 h Group); 0-h-point irradiation for 15 min, 15 min-point to 2-h darkness, 2-h-point irradiation for 15 min, darkness until 72-h (0 h + 2 h Group). As shown in Fig. 3d and e, BA release from MPB-BA solution was measured at 0 h, 2 h, 6 h, 12 h, day 1, and day 3. Results demonstrated that as irradiation time increased, the released concentration of BA increased in MPB-BA. The cumulative release percentage of BA was only 58.6 % in the dark group but increased to 65.4 % in the 0 h group and 95.4 % in the 0 h + 2 h group at 72 h, respectively (Fig. 3d, e). It has been reported that local heat could accelerate the separation of nanocarrier and drugs [53]. A plausible explanation for the increased BA release of the 0 h + 2 h group than the other groups from 6 h to 24 h was the double NIR irradiations and delayed thermal effects. Thus, we speculated that in the present work, the facilitated release of BA from MPB-BAmay be due to that local heat separated the connection between MPB and BA.

3.4. ROS scavenging activities of MPB-BA

To detect the ROS scavenging capacity of MPB-BA, total antioxidant

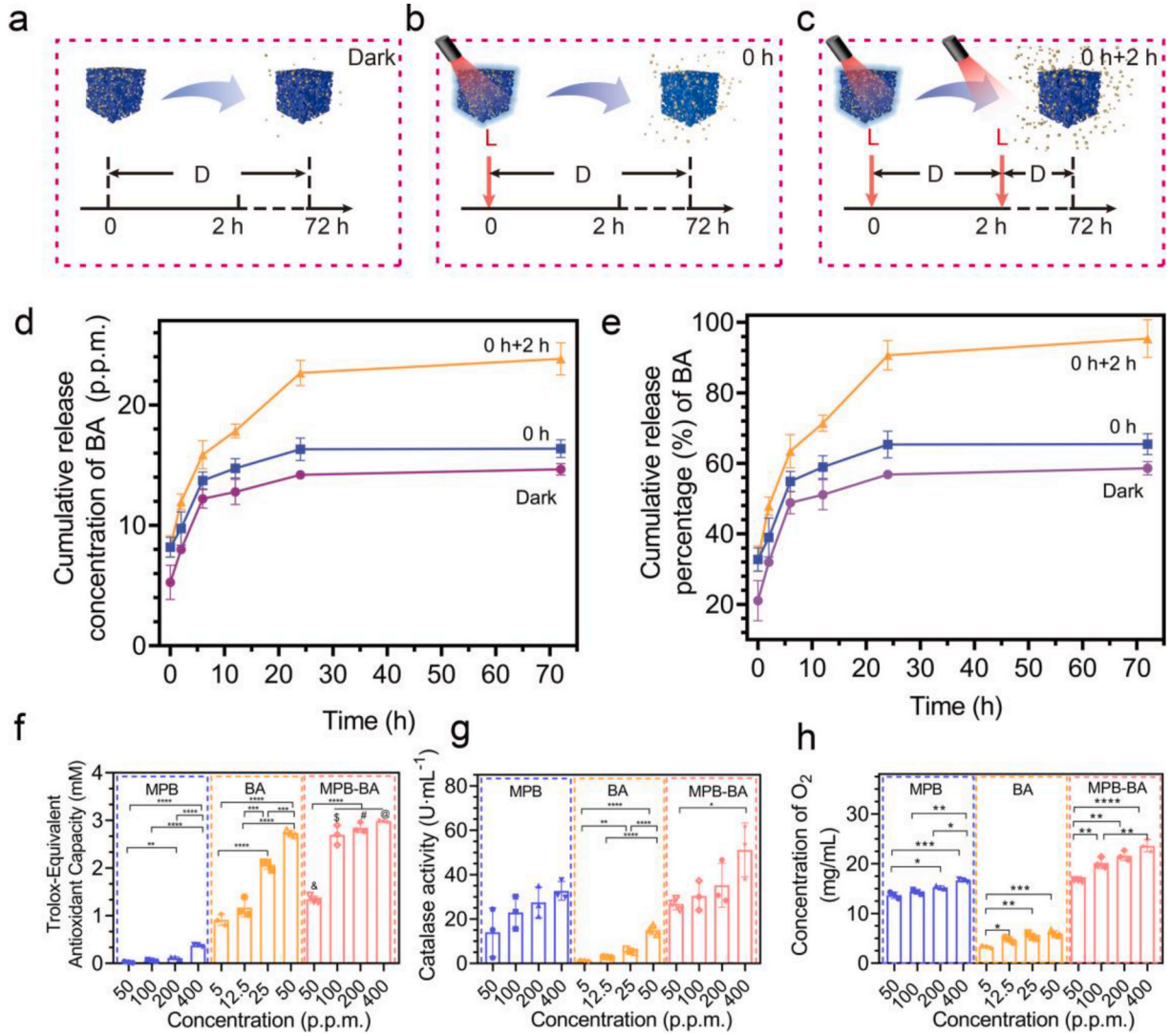

Fig. 3. NIR-controlled release of BA from MPB-BA and ROS scavenging activities of MPB-BA. (a–c) Diagrams of photothermal-controlled release performance of BA in different groups (D: dark; L: light). The subjects were distributed into 3 groups: 72-h darkness (Dark Group); 0-h-point irradiation (15 min), 15-min-point to 72-h darkness (0 h Group); 0-h-point irradiation (15 min), 15-min-point to 2-h darkness, 2-h-point irradiation (15 min), darkness until 72-h (0 h + 2 h Group). (d) Cumulative release concentration curves of BA in different groups. (e) Cumulative release percentage curves of BA in different groups. (f) Total antioxidant activity of MPB (50, 100, 200, and 400 p.p.m.), BA (5, 12.5, 25, and 50 p.p.m.) and MPB-BA (50, 100, 200, and 400 p.p.m.). (g) CAT-like activity of MPB, BA and MPB-BA. (h) O_2 generation from H_2O_2 incubation with MPB, BA and MPB-BA solution. Error bars indicated means ± standard deviations (n = 3 biologically independent samples). $^*P < 0.05$, $^{**}P < 0.01$, $^{***}P < 0.001$, $^{****}P < 0.0001$; one-way analysis of variance (ANOVA) with Dunnett's multiple comparisons test. $^{\&}$ denotes the statistical significance between MPB-BA 50 p.p.m. and MPB 50 p.p.m. ($^{\&}P < 0.0001$). $^{\$}$ denotes the statistical significance between MPB-BA 100 p.p.m. and MPB 100 p.p.m. ($^{\$}P < 0.0001$). $^{\#}$ denotes the statistical significance between MPB-BA 200 p.p.m. and MPB 200 p.p.m. ($^{\#}P < 0.0001$). $^{@}$ denotes the statistical significance between MPB-BA 400 p.p.m. and MPB 400 p.p.m. ($^{@}P < 0.0001$).

activity and catalase-like (CAT-like) activities were measured. Total antioxidant capability and CAT-like activity increased with the increase of concentration for MPB, BA, and MPB-BA (Fig. 3f, g). Both MPB and MPB-BA showed ROS scavenging activity, while MPB-BA demonstrated better antioxidant effects, compared to MPB with the same concentration. As shown in Fig. 3f, MPB-BA (100 p.p.m.) exhibited the remarkedly increased antioxidant ability. In previous studies, BA was an antioxidant and possessed excellent antioxidant properties, which was consistent with our findings [27,54]. BA (25 p.p.m.) exhibited prominent antioxidant ability, which was much higher than MPB (100 p.p.m.) (Fig. 3f). Therefore, the antioxidant ability of MPB-BA (100 p.p.m.) over MPB (100 p.p.m.) was remarkably increased mainly due to the superimposed BA and synergistic effects of MPB combined with BA. As shown in Fig. 3h, MPB and BA have an enhanced ability to promote oxygen production with growing concentrations. Particularly, MPB-BA (100, 200, and 400 p.p.m.) demonstrated better antioxidant effects, compared to MPB with the same concentration. In a word, our results showed that the ROS scavenging capacity of MPB, BA, and MPB-BA increased in a dose-dependent manner, with MPB-BA displaying the best antioxidant efficacy.

3.5. Cellular uptake study

To track the internalization of materials into cells, the particles were labeled with Cy5. The location of the cells was viewed by the stained nucleus. After incubation for 4 h, the macrophage cells showed strong red fluorescence, suggesting a significant uptake of materials by macrophage cells (Fig. S7a). The results of flow cytometry were consistent with fluorescence observation (Fig. S7b, S7c). Collectively, MPB-BA was able to enter the cell to work.

3.6. In vitro biocompatibility of MPB, BA, and MPB-BA in macrophages

Cell counting kit-8 (CCK-8) test was used to investigate the biocompatibility of MPB, BA, and MPB-BA. MPB 100 at p.p.m. and BA at 25 p.p.m were chosen for the following biological exploration owing to its superior antioxidant ability (Fig. 3f–h) combined with satisfied cytocompatibility (Fig. S8a, S8b, the detail discussions were shown in the Supporting Information). To investigate the effect of NIR light irradiation on cell viability, macrophage cells were irradiated for 15 min (initial irradiation for 5 min to reach 50 °C, maintaining 50–55 °C for 10 min) under 808 nm NIR light (Fig. S8c, S8d). Results showed that the NIR light irradiation of short duration would not impair long-term proliferative effect of macrophage cells cultured with MPB and MPB-BA (the details were discussed in the Supporting Information).

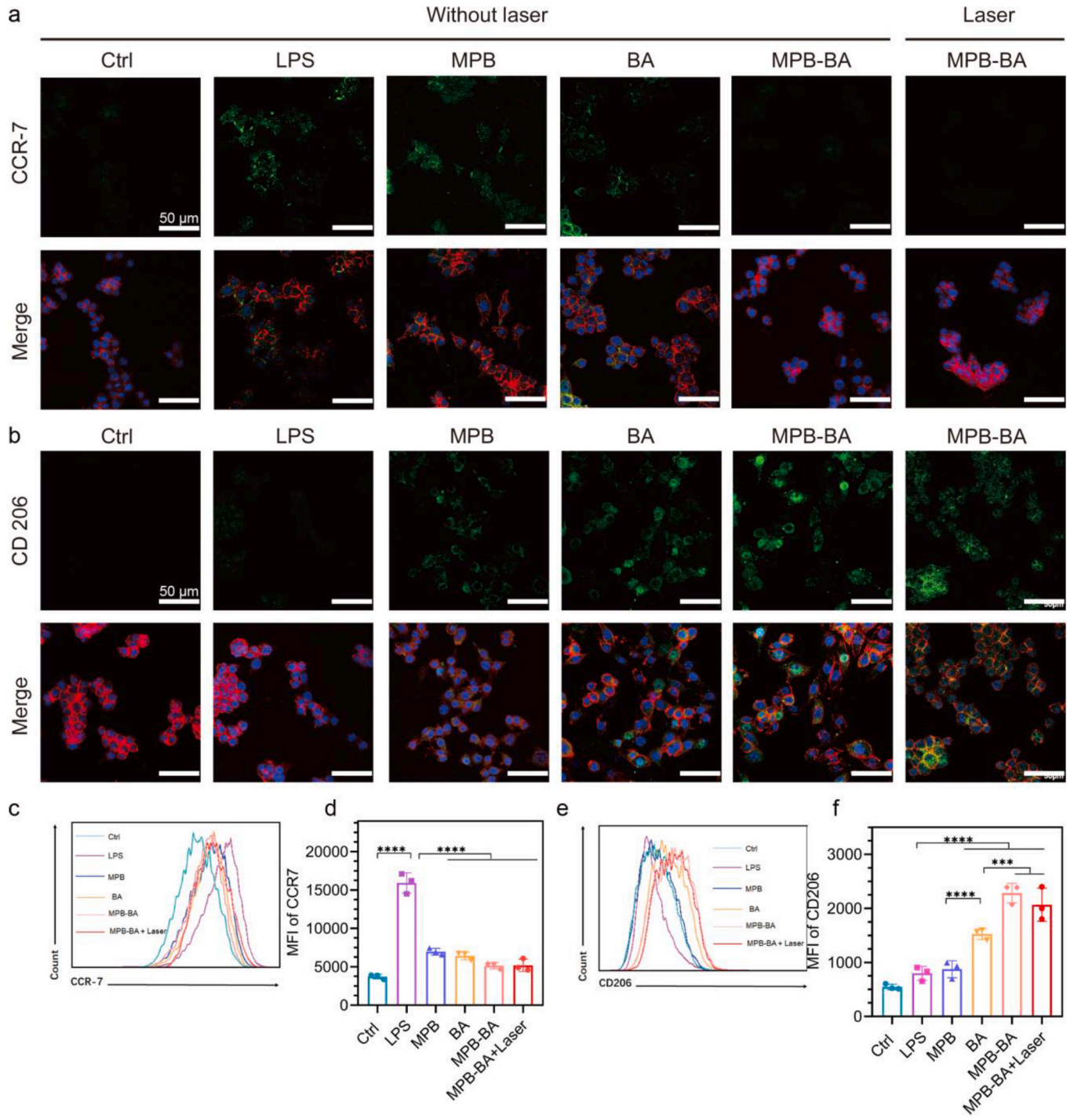

Fig. 4. The effects of MPB-BA on macrophage polarization with or without laser irradiation. Representative immunofluorescence images for CCR-7 (a, green) and CD206 (b, green) in macrophages cultured with different materials, scale bar = 50 μm. Nucleus (blue); cytoskeleton (F-actin, red). Flow cytometry results of macrophages cultured with various materials for CCR-7 (c). Quantitative analyses of the flow cytometry results of CCR-7 (d). Flow cytometry results of macrophages cultured with various materials for CD206 (e). Quantitative analyses of the flow cytometry results of CD206 (f), n =3. Error bars indicated means ± standard deviations. ***$P < 0.001$, ****$P < 0.0001$; one-way analysis of variance (ANOVA) with Dunnett's multiple comparisons test.

3.7. In vitro antibacterial efficacy of MPB-BA after laser irradiation

To investigate the antibacterial effect of different materials, the spread plate assay was performed. MPB-BA exhibited superior antibacterial effects than MPB and BA owing to synergistic actions of BA and the photothermal effects of MPB (Figs. S9a–d). To further explore the mechanism of different materials against bacterial infection, the *ortho*-nitrophenolgalactoside (ONPG) test and bacteria morphology observation by SEM were performed. It implied that the antibacterial effect of MPB-BA was fulfilled *via* destroying the integrity of bacteria and leading to the leakage of intracellular contents (Figs. S9e–j, the details were displayed in the Supporting Information). Besides, antibacterial experiments *in vivo* have been planned and will be studied in the future.

3.8. The effects of MPB-BA on macrophage polarization

Macrophages have two different phenotypes, including pro-inflammatory (M1) and anti-inflammation (M2) phenotypes. In periodontitis, the macrophages were primarily M1 phenotype that promoted inflammatory progression by secreting various pro-inflammatory cytokines [55]. Conversely, the M2 phenotype facilitates inflammation elimination by producing anti-inflammatory cytokines [19]. Therefore, switching macrophage from M1 to M2 phenotype was a potential target for drugs to exert anti-inflammatory activity. To investigate the ability of the MPB-BA for regulating macrophage polarization, immunofluorescence staining of CCR-7 (M1 marker) and CD206 (M2 marker) was performed. Increased CCR-7 signal was observed in the lipopolysaccharide (LPS) group, in which macrophage cells were simulated by LPS to induce inflammatory status. The fluorescent intensity of CCR-7 in the MPB, BA, MPB-BA and, MPB-BA with laser irradiation groups was weaker than that of the LPS group, with the fluorescent signal nearly invisible in the MPB-BA and MPB-BA with laser irradiation groups (Fig. 4a). In contrast, the intensity of CD206 in different groups was in the order of MPB-BA and MPB-BA with laser irradiation > BA > MPB > LPS (Fig. 4b). These results indicated that MPB, BA, MPB-BA and MPB-BA with laser irradiation could relieve inflammation by converting macrophage from M1 to M2 phenotype, meanwhile, MPB-BA and MPB-BA with laser irradiation revealed superior anti-inflammatory effect than the other groups. Furthermore, flow cytometry was performed to acquire a quantitative analysis of the relative fluorescence intensity of

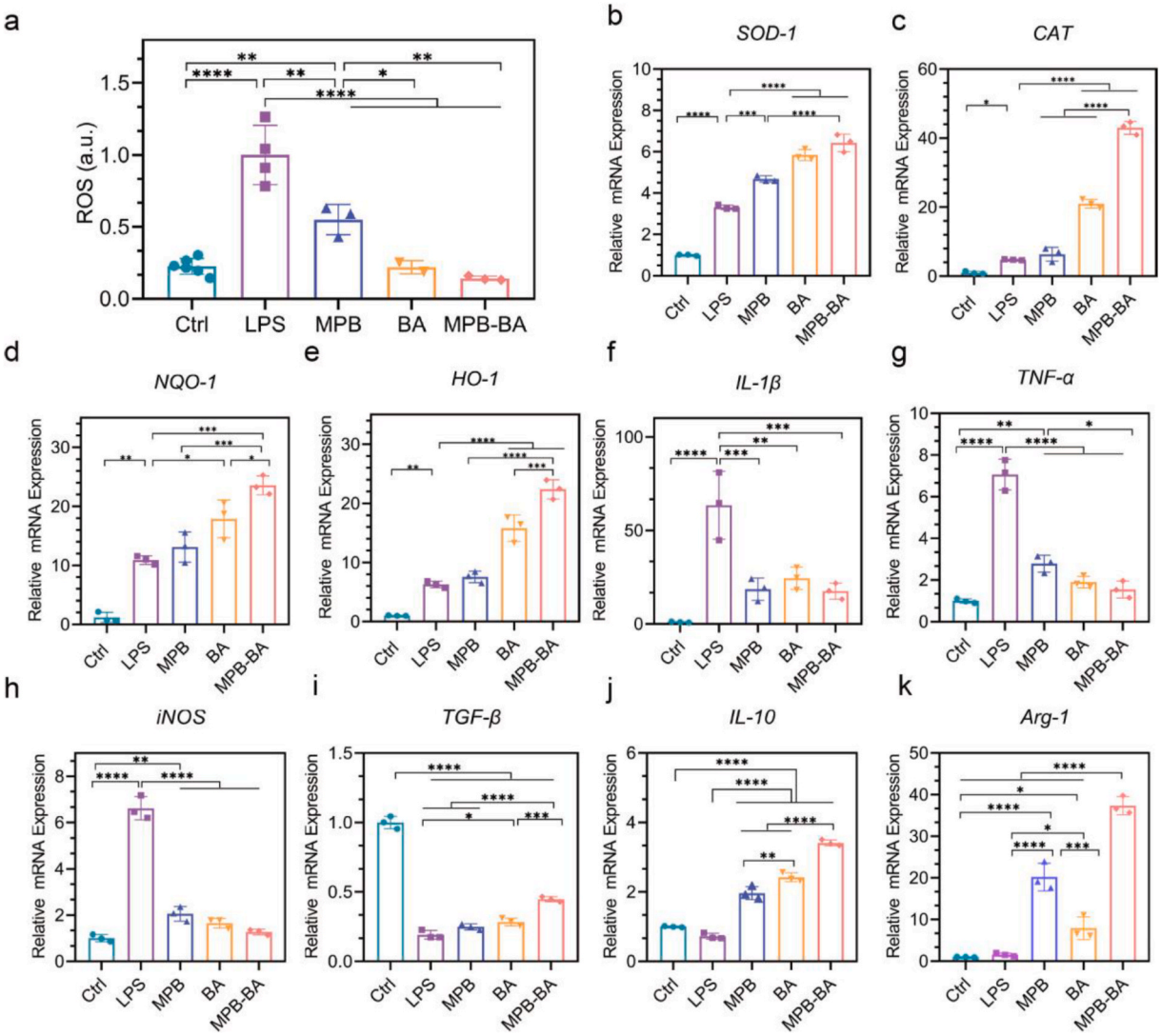

Fig. 5. *In vitro* antioxidant and anti-inflammatory effects of MPB-BA. (a) Intracellular ROS scavenging capacity of MPB (100 p.p.m.), BA (25 p.p.m.), and MPB-BA (100 p.p.m.) using DCFH-DA test. (b–e) displayed the mRNA levels of four antioxidant enzyme genes, *SOD-1*, *CAT*, *NQO-1*, and *HO-1* determined by qRT-PCR. (f–k) revealed the mRNA levels of pro-inflammatory genes *IL-1β*, *TNF-α*, *iNOS* (f–h) and anti-inflammatory genes *TGF-β*, *IL-10*, *Arg-1* (i–k), n = 3. Error bars indicated means ± standard deviations. $^{*}P < 0.05$, $^{**}P < 0.01$, $^{***}P < 0.001$, $^{****}P < 0.0001$; one-way analysis of variance (ANOVA) with Dunnett's multiple comparisons test.

CCR-7 and CD206 in various groups (Fig. 4c–f). Significantly increased CCR-7 expressions were observed in the LPS group compared to the Ctrl group. MPB-BA and MPB-BA with laser irradiation groups showed significant downregulation of CCR-7 expression and upregulation of CD206 expression, compared to the LPS group (Fig. 4c–f). Collectively, MPB-BA and MPB-BA with laser irradiation groups were most efficient in switching macrophage from M1 to M2 phenotype, which showed a potential role in the immunological therapy of periodontitis. Based on this result, we found that laser irradiation was not an essential requisite for MPB-BA to exert anti-inflammatory functions, and thereby only selected the MPB-BA group for the further mechanism study.

3.9. In vitro antioxidant and anti-inflammatory effects of MPB-BA

Oxidative stress has been considered as a pathophysiological mechanism for periodontitis. Excessive ROS leads to inflammation aggravation and intracellular constituents' damage [21]. Therefore, scavenging ROS would act as an effective approach for anti-inflammatory therapy to block the exacerbation of inflammation and protect periodontal tissue against oxidative damage. Herein, the antioxidant effects of MPB-BA in macrophages were examined by 2,7-dichlorodihydrofluorescein diacetate (DCFH-DA) assay. As shown in Fig. 5a, LPS markedly promoted ROS production to 4.4-fold of the Ctrl group. While MPB, BA, and MPB-BA decreased intracellular ROS levels compared to the LPS group. The intracellular ROS levels of the MPB-BA group were reduced by 6.8-fold to that of the LPS group.

Antioxidant enzymes played important roles in scavenging ROS [23]. Thus, the underlying molecular mechanism at the mRNA level were further explored by investigated the gene levels of antioxidant-related enzymes including *superoxide dismutase-1* (*SOD-1*), *catalase* (*CAT*), *NAD(P)H quinone dehydrogenase-1* (*NQO-1*), and *heme oxygenase-1* (*HO-1*) [56]. As shown in Fig. 5b–e, antioxidant genes in LPS-treated macrophages up-regulated compared to the Ctrl group, suggesting that cellular antioxidant defense system was activated in a high level of ROS. More importantly, antioxidant genes in MPB-BA-treated macrophages significantly increased compared to the LPS group. In the meanwhile, we found that the expression levels of *SOD-1*, *CAT*, *NQO-1*, and *HO-1* were higher in the MPB-BA group than in the MPB group. Collectively, MPB-BA enhanced the antioxidant defense capacity of macrophages by protecting against excessive oxidative stress *via* scavenging intracellular ROS and upregulating antioxidant gene levels.

Inflammatory cytokines distinctly influence the macrophage polarization [57]. To examine the effects of MPB-BA on inflammatory cytokines production in activated macrophages, gene levels of pro-inflammatory markers, including *interleukin-1beta* (*IL-1β*), *tumor necrosis factor-alpha* (*TNF-α*), *inducible nitric oxide synthase* (*iNOS*) and anti-inflammatory markers, including *transforming growth factor-beta* (*TGF-β*), *interleukin-10* (*IL-10*), *arginase-1* (*Arg-1*) were measured by qRT-PCR. These results indicated that the gene expression level of *IL-1β*, *TNF-α*, and *iNOS* upregulated significantly in the LPS group than the Ctrl group, indicating the successful establishment of the inflammatory model. As expected, MPB, BA, and MPB-BA induced downregulation of *IL-1β*, *TNF-α*, and *iNOS* gene levels, compared to the LPS group (Fig. 5f–h). In addition, BA promoted *TGF-β, IL-10* and *Arg-1* gene expression than LPS group. MPB-BA exerted the best facilitating effects on the *TGF-β*, *IL-10*, and *Arg-1* gene expression compared to the MPB and BA groups (Fig. 5i–k). Importantly, as shown in Fig. 5i, LPS decreased the expression of *TGF-β* than Ctrl group. As we know, the expression of *TGF-β* depended on the complicated local cytokine environment [58]. There were studies showed that *TGF-β* level declined in experimental periodontitis than in healthy tissue [59]. Hence, the decreased *TGF-β level* may due to complicated local cytokine environment. In summary, MPB-BA showed the best potential to alleviate inflammation among all groups.

3.10. In vitro antioxidant and anti-inflammatory mechanism of MPB-BA by regulating the Nrf2/NF-κB pathway

Nuclear transcription factor erythroid 2-related factor 2 (Nrf2) has been considered as the main regulator of oxidative stress. Activated Nrf2 could upregulate antioxidant genes (*SOD-1*, *CAT*, *NQO-1*, and *HO-1*) expression to scavenge bacteria-induced excessive ROS, which played a central role in triggering inflammatory and activating of NF-κB signal pathway [60]. ROS scavenge contributed to the inhibition of NF-κB signal pathway and then relieved of excessive inflammation and inhibit the activity of NF-κB [61]. Activation of NF-κB pathway is crucial in chronic inflammation, which is accompanied with macrophage M1 polarization and up-regulated expression of pro-inflammatory cytokines (IL-1β, TNF-α, iNOS) [62]. Our results revealed that MPB-BA shift macrophages from M1 to M2 phenotype, downregulated the pro-inflammatory gene, and upregulated the anti-inflammatory and anti-oxidant gene levels. Combined the above-mentioned results with the high involvement of Nrf2 and NF-κB in the process of oxidative stress and inflammation, we hypothesized that MPB-BA suppressed inflammation *via* regulating Nrf2/NF-κB signal pathway.

To validate our hypothesis, immunofluorescence staining and Western blot detections were performed. Immunofluorescence staining demonstrated that macrophages of the MPB-BA (−) at 30 and 60 min groups showed weak fluorescent intensity of phosphorylation of Nrf2 (*p*-Nrf2) in the cytoplasm and the nucleus after LPS-triggered inflammation (Fig. 6a). This indicated that *p*-Nrf2 showed a low expression level, suggesting that the *p*-Nrf2 was upregulated slightly in the inflammatory microenvironment owing to the activated cellular antioxidant system. Moreover, MPB-BA (+) groups at 30 and 60 min showed a stronger *p*-Nrf2 signal, mainly located in the nucleus (Fig. 6b) than the MPB-BA (−) at 30 and 60 min, which suggested that MPB-BA could promote phosphorylation of Nrf2 and the nucleus translocation of *p*-Nrf2. The fluorescence intensity of *p*-Nrf2 was analyzed quantitatively (Fig. S10a).

Furthermore, the proteins that play vital roles in the NF-κB signal pathway were also detected (Fig. 6c). Quantitative analysis of protein expression level was shown in Fig. S11. Western blot results showed that *p*-Nrf2 expression in MPB-BA (+) at 60 min was slightly higher than that in MPB-BA (+) at 30 min. With increased periods of LPS stimulation, upregulation of *p*-Nrf2 might owe to the activation of ERK1/2, Akt and JNK increase *p*-Nrf2 expression [63,64] (Fig. 6c, Fig. S11a). Higher expression of the phosphorylation of nuclear factor-kappa B P65 (p-P65) was observed in the MPB-BA (−) groups at 30 and 60 min than that at 0 min. This indicated that the NF-κB signal pathway was activated by the induction of LPS. Meanwhile, it may be an evidence that cellular antioxidant system cannot completely scavenge excessive ROS, which played a central role in the activation of NF-κB pathway. In addition, the expression of phosphorylation of I-kappa B kinase beta (*p*-IKKβ) and p-P65 in MPB-BA (+) at 30 and 60 min was lower than the MPB-BA (−) groups at 30 and 60 min, which suggested the inhibition of pro-inflammatory status. As we know, the *p*-IKKβ could promote phosphorylation and nuclear translocation of P65 to upregulate inflammation [65]. The downregulation of p-P65 may be mainly caused by the downregulation of *p*-IKKβ levels by MPB-BA, which inhibited the p-P65 nuclear translocation to induce the transcription of pro-inflammatory genes.

Collectively, MPB-BA alleviated inflammation *via* the promotion of Nrf2 phosphorylation and nuclear translocation to the inhibition of the NF-κB signal pathway. The schematic diagram of the overall molecular mechanism was shown in Fig. 6d.

3.11. In vivo biodistribution and pharmacokinetics of MPB-BA

Having investigated the therapeutic effects of MPB-BA *in vitro*, we then explored the therapeutic effects of MPB-BA *in vivo*. The anti-inflammatory function of MPB-BA was proved to be much more effective than MPB and BA *in vitro* (as shown in Figs. 4–6). Moreover, the anti-

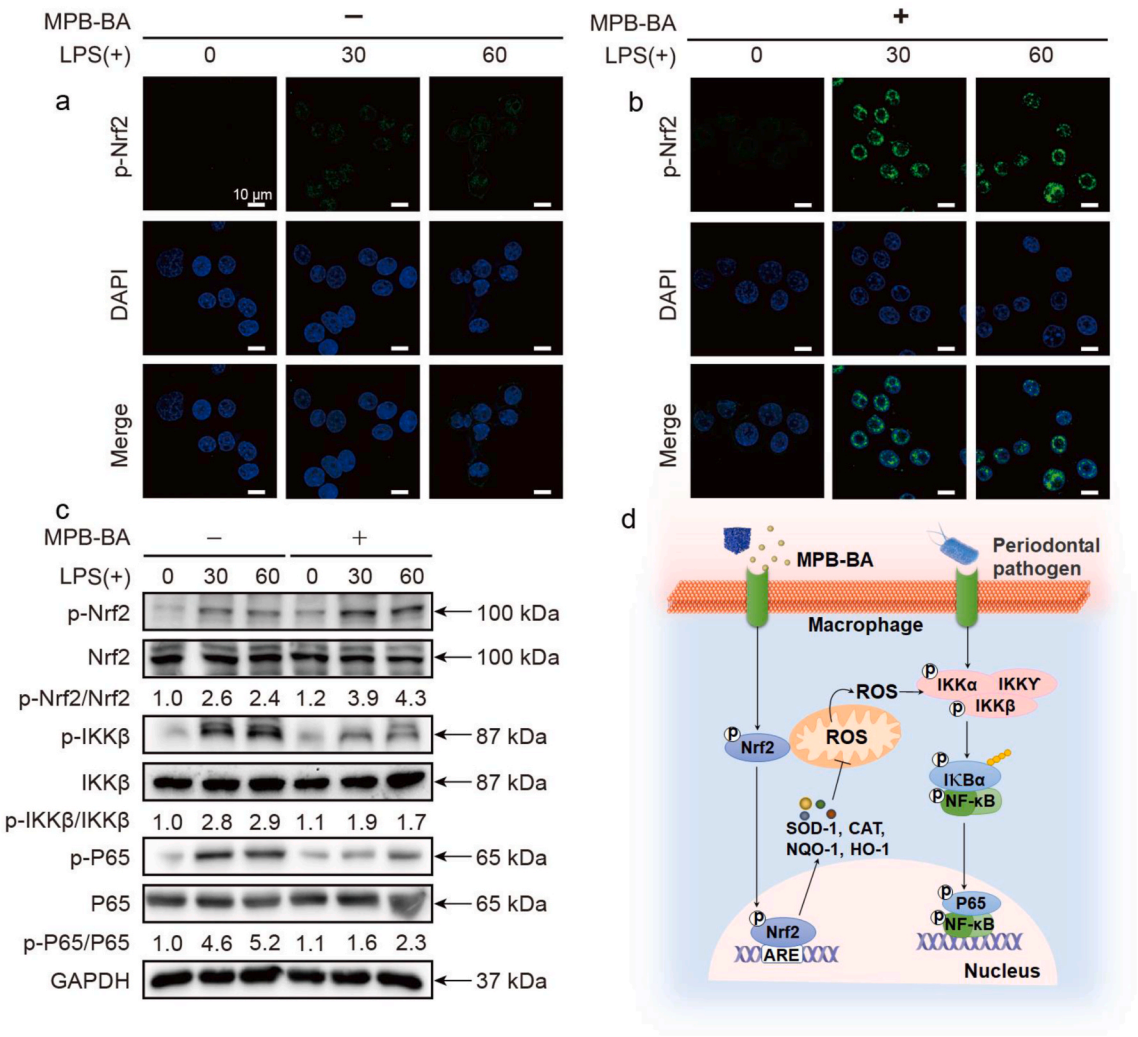

Fig. 6. *In vitro* antioxidant and anti-inflammatory mechanism evaluation of MPB-BA. Representative immunofluorescence images for *p*-Nrf2 (green) in macrophages incubated without (a) or with (b) MPB-BA before LPS treatment (0, 30, and 60 min). Nuclei were stained with DAPI (blue), scale bar = 10 μm. (c) Western blot detection of *p*-Nrf2, Nrf2 and *p*-IKKβ, IKKβ, p-P65, P65 (NF-κB inflammatory pathway), with GAPDH as the internal control. (d) The antioxidant and anti-inflammatory mechanism of MPB-BA was presented as a schematic diagram.

inflammatory mechanisms of single MPB or BA had been fully investigated in previous studies [41,66]. Therefore, we focused on MPB-BA to further explore its anti-inflammatory mechanisms *in vivo*. The treatment process using MPB-BA was shown in Figs. S12a–e. Photothermal heating images and the corresponding heating curves showed that during 808 nm laser irradiation at 1W cm^{-2}, temperature of Ctrl group did not increase and around 38 °C. Nevertheless, temperature of MPB-BA group reached to 53.7 °C for 5 min and maintain the temperature around 53.7 °C for 10 min (Fig. S13a, S13b).

We then explored the biodistribution and pharmacokinetics of MPB-BA *in vivo*. We studied the biodistribution in maxillary after 10 h applying Cy5-labeled MPB-BA *via* detecting the fluorescence by the imaging system. Fluorescence image and quantified fluorescent intensity showed that MPB-BA mainly distributed in gingiva around left maxillary dentition (Fig. S14a, S14b). The excretion of MPB-BA was studied by examining the Fe content of feces and urine using ICP-MS. As shown in Fig. S14c, S14d, MPB-BA was primarily excreted through feces. Over 60 % MPB-BA were excreted at 24 h and ~95 % of MPB-BA has been excreted at 72 h in feces, demonstrating almost none body accumulation of MPB-BA.

3.12. *In vivo* therapeutic mechanism of MPB-BA for periodontitis

We next used the transcriptomics analysis of gingival tissues of rats to further study the therapeutic mechanism. The samples were separated by applying principal components analysis (PCA), indicating the substantially different transcriptomic profiles between the MPB-BA group and the periodontitis group (Fig. 7a). The Venn diagram in Fig. 7b showed that 13,363 genes were shared by two groups, while 442 genes were exclusively expressed by the MPB-BA group. Volcano plots showed that 666 genes expressed differentially between two groups, with 327 downregulated genes and 339 upregulated genes (Fig. 7c).

Gene ontology (GO) enrichment analysis (Fig. 7d) displayed that regulation of interleukin-6 production, inflammatory response, positive regulation of immune system process, regulation of I-kappaB kinase/NF-kappaB signaling, regulation of oxidoreductase activity, regulation of superoxide metabolic process, detection of oxidative stress, superoxide-generating NADPH oxidase activity, etc., were closely related to the therapeutic mechanisms of MPB-BA for periodontitis. Kyoto Encyclopedia of Genes and Genomes (KEGG) database was further used to analyze the signaling pathway influenced by MPB-BA (Fig. 7e). It was observed that cytokine-cytokine receptor interaction, TNF signaling pathway, NF-kappaB signaling pathway, oxidative phosphorylation, etc., were highly associated with the treatment of periodontitis by MPB-

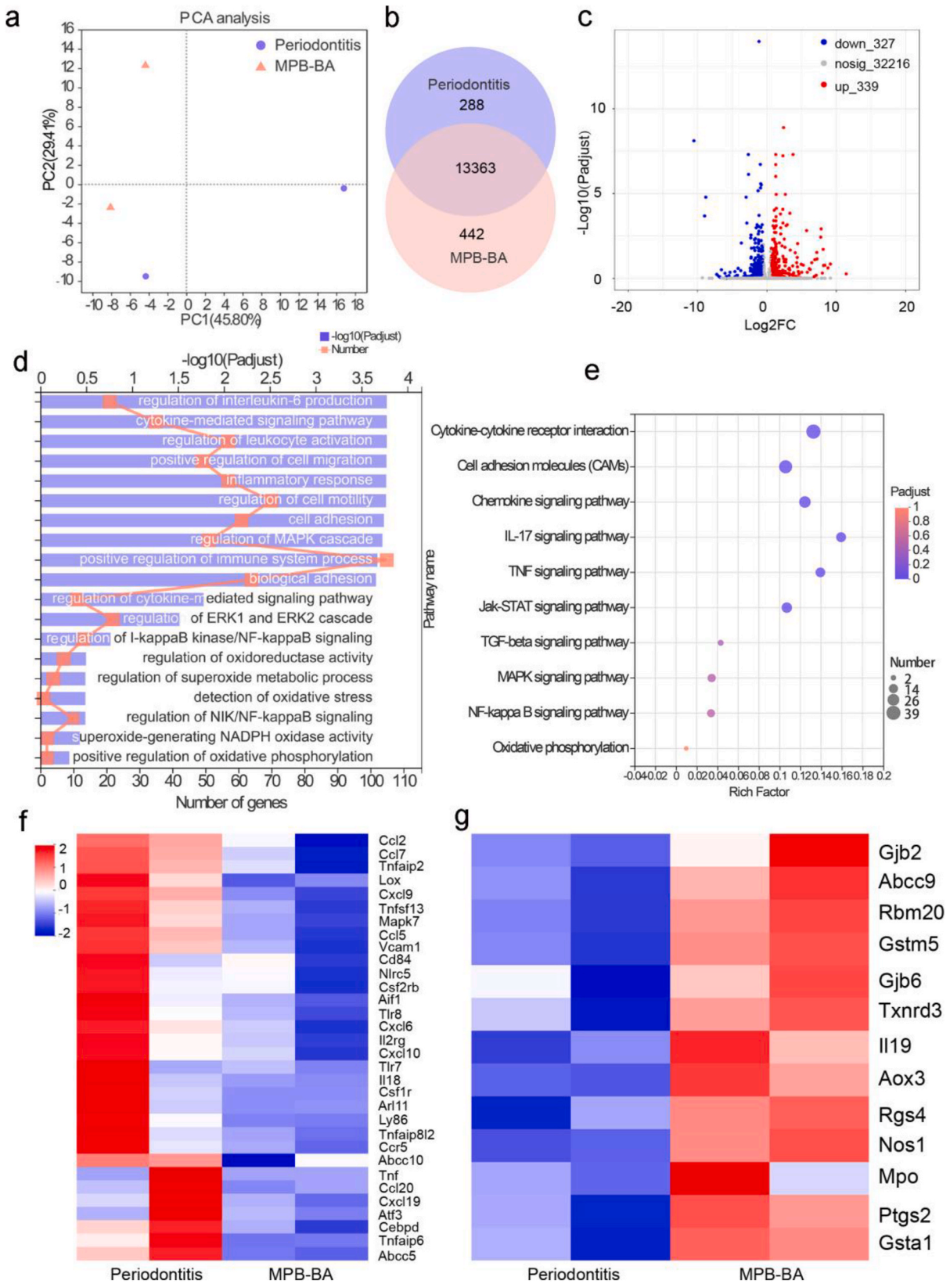

Fig. 7. *In vivo* therapeutic mechanism of MPB-BA for periodontitis. (a) Principal component analysis (PCA) was performed based on differentially expressed genes from the gingival tissue of periodontitis and MPB-BA groups. Each point represented one sample. PCA plot showed the obvious separated gene expression between periodontitis and MPB-BA groups. (b) Venn diagram of differentially expressed genes of periodontitis and MPB-BA groups. (c) Volcano plots showed the identified upregulated and downregulated genes by MPB-BA. (d) Significantly enriched GO terms for genes in the MPB-BA group compared with the periodontitis group. (e) KEGG pathway analysis for the identified differentially expressed genes. (f) Downregulated pro-inflammatory genes after MPB-BA treatment (fold change $\geq$ 1.5 and $P < 0.05$). (g) Upregulated antioxidant-related genes after MPB-BA treatment (fold change $\geq$ 1.5 and $P < 0.05$).

BA. It was observed that the NF-κB pathway, which was critical in inflammation was regulated in the MPB-BA group. The activation of the NF-κB pathway could induce M1 macrophage phenotypes and promote inflammatory molecules secretion [67]. Moreover, several oxidative stress-related pathways, including regulation of oxidoreductase activity, regulation of superoxide metabolic process, detection of oxidative stress, and superoxide-generating NADPH oxidase activity, were also influenced by MPB-BA. It is well-established that oxidative phosphorylation plays an important role in the process of respiratory chain to produce ROS [68]. The activated pathways which intimately correlated with oxidative stress may explain the therapeutic mechanism of MPB-BA for periodontitis.

Downregulated pro-inflammatory molecules treated by MPB-BA were demonstrated in Fig. 7f. Pro-inflammatory molecules such as Ccl2, Ccl5, Cxcl10, and Cxcl19 could induce M1 macrophages, which in turn secret pro-inflammatory molecules to aggravate inflammation [57]. Moreover, it was reported that the upregulation of Tnf, Il18, Tnfaip6, etc. were observed during the activation of the NF-κB pathway [62]. Our results indicated that MPB-BA may treat periodontitis *via* inhibition of the NF-κB pathway. Fig. 7g illustrated the upregulated antioxidant genes, such as *Gjb2*, *Gstm5*, *Rgs4*, *Aox3*, *Nos1*, and *Gsta1*, etc., which played a key role in scavenging ROS and protecting oxidative damage of periodontal tissue. This result implied that MPB-BA could prevent inflammation and oxidative damage by upregulated antioxidant genes

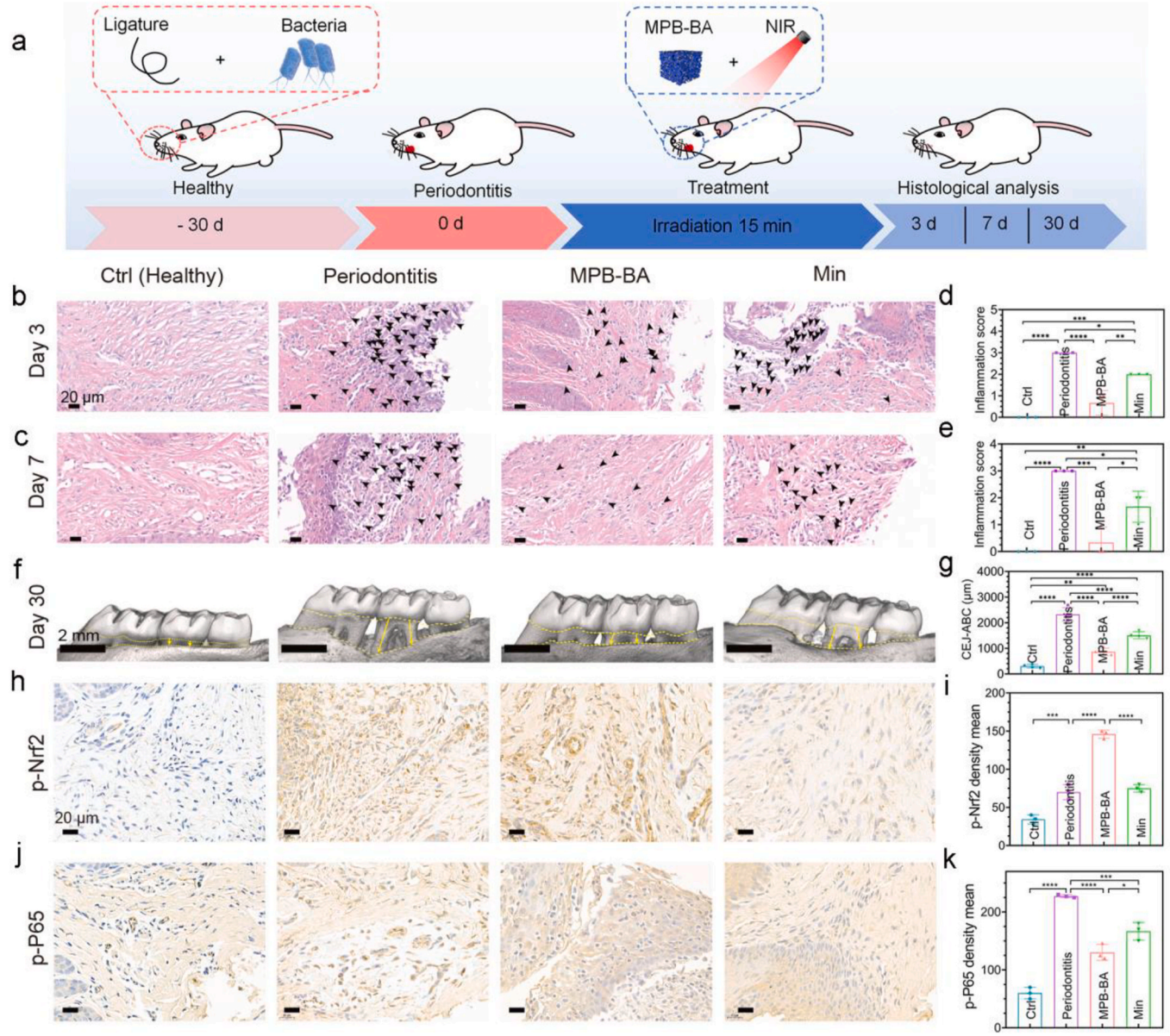

Fig. 8. *In vivo* therapeutic efficacy of MPB-BA in periodontitis rats. (a) Schematic diagram of experimental design. MPB-BA group is treated by MPB-BA and irradiated by 808 nm NIR light for 15 min. Min group is treated by a common clinical antibiotic minocycline hydrochloride. H&E staining of the periodontal tissues after 3 (b) and 7 days (c) of treatment. Black arrows indicate inflammatory cells, scale bar = 20 μm. Semi-quantitative assessment of inflammatory cells in images of H&E staining after treatment for 3 days (d) and 7 days (e). (f) Micro-CT reconstructed images of the maxillary molar area, scale bar = 2 mm. (g) The distance between the cement-enamel junction (CEJ, yellow dotted line on the top) and the crest of alveolar bone (ABC, yellow dotted line at the bottom) was measured for the first molar and second molar. (h) Immunohistochemical images of *p*-Nrf2 from different groups, scale bar = 20 μm. (i) The corresponding quantitative analysis of *p*-Nrf2 in different groups. (j) Immunohistochemical images of p-P65 from different groups, scale bar = 20 μm. (k) The corresponding quantitative analysis of p-P65 in different groups. Error bars indicated means ± standard deviations (n = 3 biologically independent samples). $^{*}P < 0.05$, $^{**}P < 0.01$, $^{***}P < 0.001$, $^{****}P < 0.0001$; one-way analysis of variance (ANOVA) with Dunnett's multiple comparisons test.

to scavenge ROS.

The above-mentioned results indicated that the underlying mechanism of MPB-BA for treatment of periodontitis may lie in the enhancement of the oxidoreductase activity, inhibition of the NF-κB pathway and subsequent increased antioxidant genes and decreased proinflammatory molecules secretion.

3.13. *In vivo* therapeutic efficacy of MPB-BA for periodontitis

The process of the animal experiment was displayed in Fig. 8a. Minocycline hydrochloride (Min) serve as the most commonly used antibiotic for current clinical treatment of periodontitis [69]. Therefore, treatment with Min was selected as a positive control, denoted as the Min group. Hematoxylin and eosin (H&E) staining was used to analyze the inflammatory cells of gingival tissue at day 3 and 7 after different treatments (Fig. 8b, c). The semi-quantitative scores of inflammatory cells after 3 and 7 days of treatments were displayed in Fig. 8d and e, respectively. On day 3, the healthy (Ctrl) group had a score of 0, which was substantially lower than the periodontitis and Min groups, with statistical significance. In addition, two treatment groups, including the MPB-BA and Min groups, both revealed lower inflammation score when compared with the periodontitis group ($P < 0.0001$ for the MPB-BA group, $P < 0.05$ for the Min group). Furthermore, the MPB-BA group exhibited lower score than that in the Min group ($P < 0.01$) (Fig. 8d). The similar tendency was observed on day 7 (Fig. 8e). *In vivo* results revealed that MPB-BA is more effective than the commonly used antibiotic Minocycline Hydrochloride for alleviating experimental periodontitis in rats.

Alveolar bone resorption was further measured by micro-CT analysis to confirm the therapeutic effects of MPB-BA for periodontitis *in vivo* (Fig. 8f). The distance between the cemento-enamel junction and the crest of the alveolar bone (CEJ-ABC) indicated that MPB-BA could block alveolar bone resorption (Fig. 8g). Since alveolar bone resorption was one of the main symptoms of periodontitis, the alleviated alveolar bone loss indicated the favorable *in vivo* therapeutic effect of MPB-BA for periodontitis.

In order to verify the *in vitro* anti-inflammatory mechanism of MPB-BA, immunohistochemical staining of *p*-Nrf2 and p-P65 were performed. The *p*-Nrf2 protein level slightly increased in the periodontitis group, which suggested that Nrf2 was activated during inflammatory status. More importantly, the MPB-BA group demonstrated higher *p*-Nrf2 protein levels than the periodontitis and Min groups, which indicated the MPB-BA treatment displayed superior antioxidant capacity than the Min application (Fig. 8h, i). In addition, higher p-P65 protein level was observed in the periodontitis group, compared with the Ctrl group, indicating the activation of NF-κB signal pathway. As accepted, the MPB-BA group revealed a lower p-P65 protein level than the periodontitis and Min groups, which suggested the excellent potential for MPB-BA to inhibit NF-κB signal pathway and alleviate inflammation (Fig. 8j, k). In summary, these results showed that MPB-BA possessed a superior *in vivo* anti-inflammatory effect than Min through regulating the Nrf2/NF-κB pathway.

The biosecurity of MPB-BA was further evaluated by H&E staining for the heart, liver, spleen, lung, and kidney (Fig. S15a). The histological sections showed that no morphological and histological change was observed in these organs between the MPB-BA group and Ctrl group after treatments for 30 days. These results indicated that the prepared MPB-BA had satisfied biosafety *in vivo*.

4. Conclusions

In this study, we developed the MPB-BA system that could exert antioxidant, anti-inflammatory, and antibacterial effects *in vitro* and *in vivo*. MPB-BA exhibited anti-inflammatory effects by altering macrophages from M1 to M2 phenotype, with decreased *IL-1β*, *TNF-α*, *iNOS*, and increased *TGF-β*, *IL-10*, *Arg-1* gene expressions. Moreover, MPB-BA also possessed antioxidant ability by upregulating antioxidant gene *SOD-1*, *CAT*, *NQO-1*, and *HO-1* expression to scavenge intracellular ROS. We further explored the underlying molecular mechanism of the MPB-BA system. Our results indicated that MPB-BA promoted the phosphorylation of Nrf2 and nucleus translocation, then consequently inhibited the activation of NF-κB signal pathway. Moreover, MPB-BA exhibited an excellent photothermal antibacterial effect against periodontal pathogens under NIR light irradiation. This study may contribute to the development of novel photothermal nanozyme-assisted immunotherapeutic strategy for bacteria-induced periodontitis by regulating Nrf2/NF-κB signaling pathway to improve oral healthcare.

CRediT authorship contribution statement

Yujuan Tian: Conceptualization, Methodology, Writing – original draft, Data curation, Investigation. **Ying Li:** Conceptualization, Writing – review & editing, Supervision, Project administration. **Jialin Liu:** Methodology, Visualization. **Yi Lin:** Methodology. **Jian Jiao:** Methodology, Visualization. **Bo Chen:** Methodology. **Wanmeng Wang:** Visualization. **Shuilin Wu:** Conceptualization, Writing – review & editing, Supervision, Project administration. **Changyi Li:** Conceptualization, Writing – review & editing, Supervision, Project administration, Funding acquisition.

Declaration of competing interest

The authors declare that they have no competing interests.

Acknowledgements

This work is jointly supported by the National Natural Science Foundation of China, Nos. 81870809, 81500886 and 31470920, and Tianjin Natural Science Foundation No. 16JCYBJC28700, Tianjin Health Science and Technology Project, ZD20021, and the China National Funds for Distinguished Young Scientists (no.51925104).

Appendix A. Supplementary data

Supplementary data to this article can be found online at https://doi.org/10.1016/j.bioactmat.2021.07.033.

References

[1] W. Marcenes, N.J. Kassebaum, E. Bernabé, A. Flaxman, M. Naghavi, A. Lopez, C. J. Murray, Global burden of oral conditions in 1990-2010: a systematic analysis, J. Dent. Res. 92 (2013) 592–597.
[2] G. Hajishengallis, Immunomicrobial pathogenesis of periodontitis: keystones, pathobionts, and host response, Trends Immunol. 35 (2014) 3–11.
[3] R.P. Darveau, Periodontitis: a polymicrobial disruption of host homeostasis, Nat. Rev. Microbiol. 8 (2010) 481–490.
[4] P. Bullon, H.N. Newman, M. Battino, Obesity, Diabetes Mellitus, Atherosclerosis and chronic periodontitis: a shared pathology *via* oxidative stress and mitochondrial dysfunction? Periodontology 2000 64 (2014) 139–153.
[5] M.K. Barton, Evidence accumulates indicating periodontal disease as a risk factor for colorectal cancer or lymphoma, Ca-Cancer, J. Clin. 67 (2017) 173–174.
[6] D.P. Miller, D.A. Scott, Inherently and conditionally essential protein catabolism genes of porphyromonas gingivalis, Trends Microbiol. 1 (2021) 54–64.
[7] E.M. Aguilera, J. Suvan, M. Orlandi, Q.M. Catalina, J. Nart, F. D'Aiuto, Association between periodontitis and blood pressure highlighted in systemically healthy individuals results from a nested case-control study, Hypertension 5 (2021) 1765–1774.
[8] B.Y. Liu, W. Bao, Maternal pre-pregnancy obesity and preterm birth: more explorations needed reply, Lancet Diabetes Endocrinol 11 (2019) 829–830.
[9] G. Hajishengallis, Periodontitis: from microbial immune subversion to systemic inflammation, Nat. Rev. Immunol. 1 (2015) 30–44.
[10] M.A. Fisher, G.W. Taylor, B.J. Shelton, K.A. Jamerson, M. Rahman, A.O. Ojo, A. R. Sehgal, Periodontal disease and other nontraditional risk factors for CKD, Am. J. Kidney Dis. 1 (2008) 45–52.
[11] R. Medzhitov, Origin and physiological roles of inflammation, Nature 454 (2008) 428–435.
[12] D.F. Kinane, P.G. Stathopoulou, P.N. Papapanou, Periodontal diseases, Nat. Rev. Dis. Primers 3 (2017) 17308.

[13] D. Graves, Cytokines, Cytokines that promote periodontal tissue destruction, J. Periodontol. 79 (2008) 1585–1591.
[14] D.F. Kinane, D.R. Demuth, S.U. Gorr, G.N. Hajishengallis, M.H. Martin, Human variability in innate immunity, Periodontology 2000 45 (2007) 14–34.
[15] G. Hajishengallis, R.J. Lamont, Beyond the red complex and into more complexity: the polymicrobial synergy and dysbiosis (PSD) model of periodontal disease etiology, Mol. Oral Microbiol. 27 (2012) 409–419.
[16] J.N. Fullerton, D.W. Gilroy, Resolution of inflammation: a new therapeutic frontier, Nat. Rev. Drug Discov. 15 (2016) 551–567.
[17] F.S.C. Sczepanik, M.L. Grossi, M. Casati, M. Goldberg, M. Glogauer, N. Fine, H. C. Tenenbaum, Periodontitis is an inflammatory disease of oxidative stress: we should treat it that way, Periodontology 2000 84 (2020) 45–68.
[18] M. Mittal, M.R. Siddiqui, K. Tran, S.P. Reddy, A.B. Malik, Reactive oxygen species in inflammation and tissue injury, Antioxidants Redox Signal. 20 (2014) 1126–1167.
[19] D.M. Mosser, J.P. Edwards, Exploring the full spectrum of macrophage activation, Nat. Rev. Immunol. 8 (2008) 958–969.
[20] H. Sies, D.P. Jones, Reactive oxygen species (ROS) as pleiotropic physiological signalling agents, Nat. Rev. Mol. Cell Biol. 21 (2020) 363–383.
[21] I.L.C. Chapple, J.B. Matthews, The role of reactive oxygen and antioxidant species in periodontal tissue destruction, Periodontology 2000 43 (2007) 160–232.
[22] T. Maruyama, T. Tomofuji, Y. Endo, K. Irie, T. Azuma, D. Ekuni, N. Tamaki, T. Yamamoto, M. Morita, Supplementation of green tea catechins in dentifrices suppresses gingival oxidative stress and periodontal inflammation, Arch. Oral Biol. 56 (2011) 48–53.
[23] S. Cuzzocrea, D.P. Riley, A.P. Caputi, D. Salvemini, Antioxidant therapy: a new pharmacological approach in shock, inflammation, and ischemia/reperfusion injury, Pharmacol. Rev. 53 (2001) 135–159.
[24] X. Li, W. Luo, T.W. Ng, P.C. Leung, C.F. Zhang, K.C.F. Leung, L.J. Jin, Nanoparticle-encapsulated baicalein markedly modulates pro-inflammatory response in gingival epithelial cells, Nanoscale 9 (2017) 12897–12907.
[25] G.M. Iova, H. Calniceanu, A. Popa, C.A. Szuhanek, O. Marcu, G. Ciavoi, I. Scrobota, The antioxidant effect of curcumin and rutin on oxidative stress biomarkers in experimentally induced periodontitis in hyperglycemic wistar rats, Molecules 26 (2021) 1332.
[26] B. Dinda, S. Dinda, S. DasSharma, R. Banik, A. Chakraborty, M. Dinda, Therapeutic potentials of baicalin and its aglycone, baicalein against inflammatory disorders, Eur. J. Med. Chem. 131 (2017) 68–80.
[27] Y. Liu, J. Shi, Antioxidative nanomaterials and biomedical applications, Nano Today 27 (2019) 146–177.
[28] L.K. Tsou, M. Lara-Tejero, J. RoseFigura, Z.J. Zhang, Y.-C. Wang, J.S. Yount, M. Lefebre, P.D. Dossa, J. Kato, F. Guan, W. Lam, Y.-C. Cheng, J.E. Galán, H. C. Hang, Antibacterial flavonoids from medicinal plants covalently inactivate type iii protein secretion substrates, J. Am. Chem. Soc. 138 (2016) 2209–2218.
[29] F. Aliakbari, H. Mohammad-Beigi, S. Abbasi, N. Rezaei-Ghaleh, F. Lermyte, S. Parsafar, S. Becker, A.P. Tafreshi, P.B. O'Connor, J.F. Collingwood, G. Christiansen, D.S. Sutherland, P.H. Jensen, D. Morshedi, D.E. Otzen, Multiple protective roles of nanoliposome-incorporated baicalein against alpha-synuclein aggregates, Adv. Funct. Mater. 31 (2021) 2007765.
[30] Y.J. Sun, L.W. Zheng, Y. Yang, X. Qian, T. Fu, X.W. Li, Z.Y. Yang, H. Yan, C. Cui, W. H. Tan, Metal-organic framework nanocarriers for drug delivery in biomedical applications, Nano-Micro Lett. 12 (2020) 103.
[31] N. Zhang, X. Cai, W. Gao, R. Wang, C. Xu, Y. Yao, L. Hao, D. Sheng, H. Chen, Z. Wang, Y. Zheng, A multifunctional theranostic nanoagent for dual-mode image-guided HIFU/chemo- synergistic cancer therapy, Theranostics 6 (2016) 404–417.
[32] K. Zhang, M. Tu, W. Gao, X. Cai, F. Song, Z. Chen, Q. Zhang, J. Wang, C. Jin, J. Shi, X. Yang, Y. Zhu, W. Gu, B. Hu, Y. Zheng, H. Zhang, M. Tian, Hollow Prussian blue nanozymes drive neuroprotection against ischemic stroke via attenuating oxidative stress, counteracting inflammation, and suppressing cell apoptosis, Nano Lett. 19 (2019) 2812–2823.
[33] X. Cai, W. Gao, M. Ma, M. Wu, L. Zhang, Y. Zheng, H. Chen, J. Shi, A Prussian blue-based core-shell hollow-structured mesoporous nanoparticle as a smart theranostic agent with ultrahigh pH-responsive longitudinal relaxivity, Adv. Mater. 27 (2015) 6382–6389.
[34] X. Cai, X. Jia, W. Gao, K. Zhang, M. Ma, S. Wang, Y. Zheng, J. Shi, H. Chen, A versatile nanotheranostic agent for efficient dual-mode imaging guided synergistic chemo-thrmal tumor therapy, Adv. Funct. Mater. 25 (2015) 2520–2529.
[35] Y. Xu, Y. Zhang, X. Cai, W. Gao, X. Tang, Y. Chen, J. Chen, L. Chen, Q. Tian, S. Yang, Y. Zheng, B. Hu, Large-scale synthesis of monodisperse Prussian blue nanoparticles for cancer theranostics *via* an "in situ modification" strategy, Int. J. Nanomed. 14 (2019) 271–288.
[36] X. Jia, X. Cai, Y. Chen, S. Wang, H. Xu, K. Zhang, M. Ma, H. Wu, J. Shi, H. Chen, Perfluoropentane-encapsulated hollow mesoporous prussian blue nanocubes for activated ultrasound imaging and photothermal therapy of cancer, ACS Appl. Mater. Interfaces 7 (2015) 4579–4588.
[37] L. Feng, C. Dou, Y. Xia, B. Li, M. Zhao, P. Yu, Y. Zheng, A.M. El-Toni, N.F. Atta, A. Galal, Y. Cheng, X. Cai, Y. Wang, F. Zhang, Neutrophil-like cell-membrane-coated nanozyme therapy for ischemic brain damage and long-term neurological functional recovery, ACS Nano 15 (2021) 2263–2280.
[38] W. Hou, C. Ye, M. Chen, W. Gao, X. Xie, J. Wu, K. Zhang, W. Zhang, Y. Zheng, X. Cai, Excavating bioactivities of nanozyme to remodel microenvironment for protecting chondrocytes and delaying osteoarthritis, Bioactive materials 6 (2021) 2439–2451.
[39] X. Cai, K. Zhang, X. Xie, X. Zhu, J. Feng, Z. Jin, H. Zhang, M. Tian, H. Chen, Self-assembly hollow manganese Prussian white nanocapsules attenuate Tau-related neuropathology and cognitive decline, Biomaterials 231 (2020) 119678.
[40] J. Zhao, X. Cai, W. Gao, L. Zhang, D. Zou, Y. Zheng, Z. Li, H. Chen, Prussian blue nanozyme with multienzyme activity reduces colitis in mice, ACS Appl. Mater. Interfaces 10 (2018) 26108–26117.
[41] X. Xie, J. Zhao, W. Gao, J. Chen, B. Hu, X. Cai, Y. Zheng, Prussian blue nanozyme-mediated nanoscavenger ameliorates acute pancreatitis via inhibiting TLRs/NF-κB signaling pathway, Theranostics 11 (2021) 3213–3228.
[42] L. Feng, C. Dou, Y. Xia, B. Li, M. Zhao, A.M. El-Toni, N.F. Atta, Y. Zheng, X. Cai, Y. J. Wang, Enhancement of nanozyme permeation by endovascular interventional treatment to prevent vascular restenosis via macrophage polarization modulation, Adv. Funct. Mater. 30 (2020) 2006581.
[43] J. Zhao, W. Gao, X. Cai, J. Xu, D. Zou, Z. Li, B. Hu, Y. Zheng, Nanozyme-mediated catalytic nanotherapy for inflammatory bowel disease, Theranostics 9 (2019) 2843–2855.
[44] F. Graziani, D. Karapetsa, B. Alonso, D. Herrera, Nonsurgical and surgical treatment of periodontitis: how many options for one disease? Periodontology 2000 75 (2017) 152–188.
[45] D. Han, Y. Li, X. Liu, B. Li, Y. Han, Y. Zheng, K.W.K. Yeung, C. Li, Z. Cui, Y. Liang, Rapid bacteria trapping and killing of metal-organic frameworks strengthened photo-responsive hydrogel for rapid tissue repair of bacterial infected wounds, Chem. Eng. J. 396 (2020) 125194.
[46] J. Li, X. Liu, L. Tan, Z. Cui, X. Yang, Y. Liang, Z. Li, S. Zhu, Y. Zheng, K.W.K. Yeung, X. Wang, S. Wu, Zinc-doped prussian blue enhances photothermal clearance of staphylococcus aureus and promotes tissue repair in infected wounds, Nat. Commun. 10 (2019) 4490.
[47] X. Xie, W. Gao, J. Hao, J. Wu, X. Cai, Y. Zheng, Self-synergistic effect of Prussian blue nanoparticles for cancer therapy: driving photothermal therapy and reducing hyperthermia-induced side effects, J. Nanobiotechnol. 19 (2021) 126.
[48] T. Feng, J. Wan, P. Li, H. Ran, H. Chen, Z. Wang, L. Zhang, A novel NIR-controlled NO release of sodium nitroprusside-doped Prussian blue nanoparticle for synergistic tumor treatment, Biomaterials 214 (2019) 119213.
[49] X. Cai, W. Gao, L. Zhang, M. Ma, T. Liu, W. Du, Y. Zheng, H. Chen, J. Shi, Enabling Prussian blue with tunable localized surface plasmon resonances: simultaneously enhanced dual-mode imaging and tumor photothermal therapy, ACS Nano 10 (2016) 11115–11126.
[50] Y. Almoshari, R. Ren, H. Zhang, Z. Jia, X. Wei, N. Chen, G. Li, S. Ryu, S.M. Lele, R. A. Reinhardt, D. Wang, GSK3 Inhibitor-loaded osteotropic pluronic hydrogel effectively mitigates periodontal tissue damage associated with experimental periodontitis, Biomaterials 261 (2020) 120293.
[51] W. Lee, A. Permatasari, B.W. Kwon, Y. Kwon, Performance evaluation of aqueous organic redox flow battery using anthraquinone-2,7-disulfonic acid disodium salt and potassium iodide redox couple, Chesm. Eng. J. 358 (2019) 1438–1445.
[52] D.H. Zhu, G.W. Huang, L.Y. Zhang, Y. He, H.Q. Xie, W. Yu, Silver nanowires contained nanofluids with enhanced optical absorption and thermal transportation properties, Energy Environ. Mater. 1 (2019) 22–29.
[53] R. Weinstain, T. Slanina, D. Kand, P. Klán, Visible-to-NIR-light activated release: from small molecules to nanomaterials, Chem. Rev. 120 (2020) 13135–13272.
[54] Q. Zhao, Y. Zhang, G. Wang, L. Hill, J.K. Weng, X.Y. Chen, H.W. Xue, C. Martin, A specialized flavone biosynthetic pathway has evolved in the medicinal plant, Scutellaria baicalensis, Sci. Adv. 4 (2016) 15.
[55] Y. Sun, X.L. Sun, X. Li, W. Li, C.Y. Li, Y.M. Zhou, L. Wang, B. Dong, A versatile nanocomposite based on nanoceria for antibacterial enhancement and protection from aPDT-aggravated inflammation *via* modulation of macrophage polarization, Biomaterials 268 (2021) 120614.
[56] T.W. Kensler, N. Wakabayash, S. Biswal, Cell survival responses to environmental stresses *via* the Keap1-Nrf2-ARE pathway, Annu. Rev. Pharmacol. Toxicol. 47 (2007) 89–116.
[57] A. Mantovani, A. Sica, S. Sozzani, P. Allavena, A. Vecchi, M. Locati, The chemokine system in diverse forms of macrophage activation and polarization, Trends Immunol. 25 (2004) 677–686.
[58] M.A. Travis, D. Sheppard, TGF-β activation and function in immunity, Annu. Rev. Immunol. 32 (2014) 51–82.
[59] U. Skaleric, B. Kramar, M. Petelin, Z. Pavlica, S.M. Wahl, Changes in TGF-beta 1 levels in gingiva, crevicular fluid and serum associated with periodontal inflammation in humans and dogs, Eur. J. Oral Sci. 2 (1997) 136–142.
[60] Q. Ma, Role of Nrf2 in oxidative stress and toxicity, Annu. Rev. Pharmacol. Toxicol. 53 (2013) 401–426.
[61] M.J. Morgan, Z.G. Liu, Crosstalk of reactive oxygen species and NF-Kappa B signaling, Cell Res. 21 (2011) 103–115.
[62] T. Lawrence, The Nuclear Factor NF-KappaB pathway in inflammation, Cold Spring Harbor Perspect. Biol. 1 (2009) a001651.
[63] F. Correa, C. Mallard, M. Nilsson, M. Sandberg, Activated microglia decrease histone acetylation and Nrf2-inducible anti-oxidant defence in astrocytes: restoring effects of inhibitors of HDACs, p38 MAPK and GSK3β, Neurobiol. Dis. 1 (2011) 142–151.
[64] F. Correa, E. Ljunggren, C. Mallard, M. Nilsson, S.G. Weber, M. Sandberg, The Nrf2-inducible antioxidant defense in astrocytes can be both up- and down-regulated by activated microglia: involvement of p38 MAPK, Glia 5 (2011) 785–799.
[65] A.A. Zarrin, K. Bao, P. Lupardus, D. Vucic, Kinase inhibition in autoimmunity and inflammation, Nat. Rev. Drug Discov. 20 (2021) 39–63.
[66] Z.J. Zhang, W. Cui, G.H. Li, S. Yuan, D.P. Xu, M.P.M. Hoi, Z.X. Lin, J. Dou, Y. F. Han, S.M.Y. Lee, Baicalein protects against 6-OHDA-induced neurotoxicity through activation of keap1/nrf2/HO-1 and involving PKC alpha and PI3K/AKT signaling pathways, J. Agric. Food Chem. 33 (2012) 8171–8182.

[67] M.G. Dorrington, I.D.C. Fraser, NF-κB signaling in macrophages: dynamics, crosstalk, and signal integration, Front. Immunol. 10 (2019) 705.
[68] E.L. Mills, B. Kelly, A. Logan, A.S.H. Costa, M. Varma, C.E. Bryant, P. Tourlomousis, J.H.M. Däbritz, E. Gottlieb, I. Latorre, S.C. Corr, G. McManus, D. Ryan, H.T. Jacobs, M. Szibor, R.J. Xavier, T. Braun, C. Frezza, M.P. Murphy, L.A. O'Neill, Succinate dehydrogenase supports metabolic repurposing of mitochondria to drive inflammatory macrophages, Cell 24 (2016) 457–470.
[69] M.F. Timmerman, G.A.v.d. Weijden, T.J.v. Steenbergen, M.S. Mantel, J.d. Graaff, U.v.d. Velden, Evaluation of the long-term efficacy and safety of locally-applied minocycline in adult periodontitis patients, J. Clin. Periodontol. 23 (1996) 707–716.